Nuclear shell structure in a finite-temperature relativistic framework

Herlik Wibowo ¹,* and Elena Litvinova ²,3,4

¹Institute of Physics, Academia Sinica, Taipei 11529, Taiwan

²Department of Physics, Western Michigan University, Kalamazoo, Michigan 49008, USA

³National Superconducting Cyclotron Laboratory, Michigan State University, East Lansing, Michigan 48824, USA

⁴GANIL, CEA/DRF-CNRS/IN2P3, F-14076 Caen, France



(Received 12 October 2021; revised 3 August 2022; accepted 22 August 2022; published 10 October 2022)

The shell evolution of neutron-rich nuclei with temperature is studied in a beyond-mean-field framework rooted in the meson-nucleon Lagrangian. The temperature-dependent Dyson equation with a dynamical kernel taking into account the particle-vibration coupling (PVC) is solved for the fermionic propagators in the basis of the thermal relativistic mean-field Dirac spinors. The calculations are performed for $^{68-78}$ Ni in a broad range of temperatures $0 \le T \le 4$ MeV. Special focus is put on the fragmentation pattern of the single-particle states, which is further investigated within toy models in truncated model spaces. Such models allow for quantifying the sensitivity of the fragmentation to the phonon frequencies, the PVC strength, and the mean-field level density. This study provides insights into the temperature evolution of the PVC mechanism in real nuclear systems under the conditions which occur in astrophysical environments. In this connection, we discuss the temperature-dependent nucleon effective mass and symmetry energy coefficient, which are key ingredients of the nuclear equation of state.

DOI: 10.1103/PhysRevC.106.044304

I. INTRODUCTION

Understanding the behavior of atomic nuclei and nuclear matter at finite temperature is extremely important for advancements at the frontiers of nuclear science. The modification of in-medium nucleonic correlations with temperature changes considerably the nuclear structure, leading to the transition to the nonsuperfluid phase, weakening of collective effects, the appearance of shape fluctuations, and the formation of new structures in the excitation spectra due to thermal unblocking [1-6]. Microscopic interpretation of these phenomena is crucial for accurate predictions of nuclear processes in astrophysical environments, such as neutron star mergers and supernovae [7-12]. As found in the recent studies of Refs. [6,13], the emergent effects of many-body correlations, of both collective and noncollective origin, play a decisive role in the key nuclear reaction rates employed in r-process nucleosynthesis and core-collapse supernovae (CCSN) simulations. Precise knowledge of the evolution of nuclear emergent phenomena with temperature is, therefore, mandatory for a high-quality nuclear physics input utilized in astrophysical modeling [7,14–16].

The equation of motion (EOM) method builds a systematic framework for the description of many-body correlations, in particular, in strongly coupled fermionic systems [17–22]. Within this framework, EOMs are generated for various time-dependent quantities, such as the correlation functions of field operators. One of the simplest correlation functions is the

fermionic propagator through the correlated medium, which is directly related to the energies of quasiparticles and their occupancies of the basis orbitals [23,24]. In principle, the single-particle propagators of the states below the Fermi energy define completely the total ground state energy of the system, if the underlying Hamiltonian is confined by the two-body interaction, via the Midgal-Galitski-Koltun sum rule [25,26]. This fact is, in turn, in compliance with the density functional theory, where the total ground state energy is defined by the one-body density, which is the static limit of the single-particle propagator. Thus, the correlated one-body propagator plays a fundamental role in the description of quantum many-body systems.

However, the exact EOM for the one-body propagator does not have a closed form. Instead, it contains higher-rank propagators in the dynamical part of the interaction kernel, namely, the two-body propagator in the nonsymmetric form and the three-body propagator in the symmetric form of this kernel [27,28]. This requires external EOMs for the latter propagators, which, in turn, are coupled to even higher-rank ones through the more complex dynamical kernels, leading to a hierarchy of coupled EOMs. In nuclear physics applications, however, quantitatively most important coupling is the one between the one-body and two-body propagators, while the two-body EOM can be formulated in various approximations which allow one to truncate the hierarchy of EOMs on a certain level with a reasonable accuracy.

The simplest descriptions of quantum many-body systems take the dynamical kernels of the EOMs into account in static approximations. Such descriptions are confined by one-body densities and propagators and include the Hartree-Fock

^{*}herlik.wibowo@york.ac.uk

approach [29–31], the random phase approximation (RPA) [32], the Gor'kov theory of superfluidity [33], and the Bardeen-Cooper-Schrieffer (BCS) model [34], to name a few. Needless to say, such approximations neglect the explicit coupling between the one-body and two-body EOM's and, thus, are insufficient for an accurate description of nuclear phenomena, which is required for modern applications and for a deep understanding of emergent effects. A better accuracy can be achieved by cluster expansions of the dynamical kernels of both the one-body and two-body fermionic EOMs in terms of the two-time two-body correlation functions, as discussed, e.g., in the context of condensed matter and quantum chemistry applications [17–19,21]. For the nuclear physics calculations, possible truncation schemes of the dynamical kernels on the two-body level were discussed, for instance, in Ref. [27]. The great advantage of the EOM method is that both the static and dynamical kernels are derived consistently from the same underlying bare interaction. In nuclear physics, however, the implementations of EOM-based methods with dynamical kernels still mainly employ effective interactions.

Early approaches postulated phenomenological Hamiltonians implying the existence of fermionic quasiparticles and phonons of a bosonic origin [35–43]. In such approaches the effective residual interaction between fermions is supplemented by the phonon-exchange interaction, or (quasi)particle-vibration coupling [(q)PVC]. Relatively simple calculation schemes are possible with the use of effective phenomenological interactions; however, more accurate and sophisticated versions of PVC were successfully implemented over the years [27,44–52]. The models, which operate mostly the phonon degrees of freedom [40–43], include correlations of high complexity, and a few attempts using bare nucleon-nucleon interactions were reported [53–56].

In this work we examine the EOM for the one-body propagator, which is, in its most general form, the Dyson equation. We consider the finite-temperature case and employ the approach developed in Ref. [57] as an extension of the zero-temperature PVC model [58,59]. These approaches are both built upon relativistic quantum hadrodynamics [60–63], adopting the PVC mechanism [27,64-66] for the induced interaction. As follows from Refs. [27,65], PVC is the leading contribution to the one-fermion dynamical kernel, or the self-energy, in finite nuclei. Qualitatively similar to the phenomenological PVC proposed quite early by Bohr and Mottelson [35,36], further developed in Refs. [64,67–72] and later in self-consistent approaches [58,59,73,74], it is now understood in terms of the EOM derived from bare nucleonnucleon interactions [27,28]. In this work we still keep the phenomenological effective interaction adjusted in the framework of the covariant density functional theory (CDFT) [63] for the static part of the EOM kernel and the PVC, that allows one to obtain the PVC vertices and phonon propagators within the relativistic random phase approximation (RRPA) with good accuracy. This feature remains intact also at finite temperature, which is another important ingredient of our present study. We focus on a systematic application of the approach to the temperature evolution of the PVC mechanism in the neutron-rich even-even nuclei ^{68–78}Ni, which are of interest for various astrophysical applications. These nuclei represent a

high-sensitivity region of the nuclear chart for both r-process nucleosynthesis and CCSN. In particular, the PVC effects are responsible for a nontrivial behavior of the nucleon effective mass and symmetry energy, and this connection propagates to a non-negligible temperature dependence of these quantities in stellar environments with sizable impacts on the stellar evolution [14,15,75–77].

II. DYSON EQUATION FOR THE FERMIONIC PROPAGATOR AT FINITE TEMPERATURE

We define the hot nucleus as a system of Dirac nucleons moving in a self-consistent field generated by an effective meson-nucleon interaction at finite temperature. The electromagnetic interaction between protons is mediated by the photon. One of the most convenient ways to quantify the single-particle motion in a fermionic many-body system is to evaluate the one-fermion propagator (also called Green function), which describes the motion of a fermion through the correlated medium formed by N identical interacting fermions. The advantage of such a description is the simple relationship of this propagators to the excitation spectra and ground-state properties of the systems with (N + 1) and (N-1) fermions. In this work we are interested in nuclear systems in thermal equilibrium with the surroundings, that can be associated with a certain temperature. The temperature, or Matsubara, propagator of a fermion is defined as [78–80]

$$\mathscr{G}(1,1') \equiv \mathscr{G}_{k_1 k_{1'}}(\tau_1 - \tau_{1'}) = -\langle T_\tau \psi(1) \overline{\psi}(1') \rangle, \qquad (1)$$

where the angular brackets stand for the thermal average [79,80] and the chronological ordering operator T_{τ} acts on the fermionic field operators in the Wick-rotated picture:

$$\psi(1) \equiv \psi_{k_1}(\tau_1) = e^{\mathcal{H}\tau_1} \psi_{k_1} e^{-\mathcal{H}\tau_1},$$

$$\overline{\psi}(1) \equiv \psi_{k_1}^{\dagger}(\tau_1) = e^{\mathcal{H}\tau_1} \psi_{k_1}^{\dagger} e^{-\mathcal{H}\tau_1}.$$
(2)

In Eq. (2), the evolution is determined by the operator $\mathcal{H} = H - \mu N$, where H is the many-body Hamiltonian, μ is the chemical potential, and N denotes the particle number. The subscript k_1 defines the full set of the single-particle quantum numbers in a given representation, while the imaginary time variable τ is related to the real time t as $\tau = it$. The fermionic fields ψ_{k_1} and $\psi_{k_1}^{\dagger}$ satisfy the usual anticommutation relations.

For the many-body Hamiltonian H containing only the free-motion and the mean-field contributions, i.e., confined by the one-body part, the single-fermion Matsubara Green function reads

$$\widetilde{\mathscr{G}}(2,1) = \sum_{\sigma=\pm 1} \widetilde{\mathscr{G}}^{\sigma}(2,1),$$

$$\widetilde{\mathscr{G}}^{\sigma}(2,1) = -\sigma \delta_{k_2 k_1} n(-\sigma(\varepsilon_{k_1} - \mu), T) e^{-(\varepsilon_{k_1} - \mu)\tau_{21}} \theta(\sigma \tau_{21}),$$
(3)

where $\tau_{21} = \tau_2 - \tau_1$ and ε_{k_1} are the eigenvalues of the single-particle Hamiltonian diagonal in the $\{k_i\}$ basis. Accordingly, $n(\varepsilon, T)$ is the Fermi-Dirac distribution

$$n(\varepsilon, T) = \frac{1}{\exp(\varepsilon/T) + 1} \tag{4}$$

at the temperature T and characterizes the mean-field occupancies of the orbits with the given single-particle energies. The Fourier transform of the propagator (3) to the energy domain,

$$\widetilde{\mathscr{G}}_{k_2k_1}(\varepsilon_\ell) = \int_0^{1/T} d\tau e^{i\varepsilon_\ell \tau} \widetilde{\mathscr{G}}_{k_2k_1}(\tau), \tag{5}$$

leads to its spectral representation

$$\widetilde{\mathscr{G}}_{k_2k_1}(\varepsilon_\ell) = \delta_{k_2k_1}\widetilde{\mathscr{G}}_{k_1}(\varepsilon_\ell), \quad \widetilde{\mathscr{G}}_{k_1}(\varepsilon_\ell) = \frac{1}{i\varepsilon_\ell - \varepsilon_{k_1} + \mu}, \quad (6)$$

defined at the discrete Matsubara frequencies ε_{ℓ} ,

$$\varepsilon_{\ell} = (2\ell + 1)\pi T,\tag{7}$$

with the integer ℓ . In Eqs. (3)–(6) we indicate the mean-field character of the respective Green function by the "symbol."

The presence of two-body and higher-rank terms in the many-body Hamiltonian induce correlations beyond mean field originated from the residual interaction. The correlated propagator can be found as a solution of the Dyson equation

$$\mathcal{G}_{k_1 k_2}(\varepsilon_{\ell}) = \widetilde{\mathcal{G}}_{k_1 k_2}(\varepsilon_{\ell}) + \sum_{k_2 k_4} \widetilde{\mathcal{G}}_{k_1 k_3}(\varepsilon_{\ell}) \Sigma_{k_3 k_4}^{\ell}(\varepsilon_{\ell}) \mathcal{G}_{k_4 k_2}(\varepsilon_{\ell}), \quad (8)$$

where the energy-dependent mass operator (i.e., self-energy) Σ^e describes the coupling between single fermions and inmedium emergent degrees of freedom. In this work, we employ the PVC model for Σ^e , which approximates the exact energy-dependent self-energy Σ^e by a cluster expansion truncated at the two-body level [27]. This self-energy, in the leading approximation, reads

$$\Sigma_{k_1 k_2}^{e}(\varepsilon_{\ell}) = -T \sum_{k_3, m} \sum_{\ell'} \sum_{\sigma = \pm 1} \widetilde{\mathscr{G}}_{k_3}(\varepsilon_{\ell'}) \frac{\sigma g_{k_1 k_3}^{m(\sigma)} g_{k_2 k_3}^{m(\sigma)*}}{i \varepsilon_{\ell} - i \varepsilon_{\ell'} - \sigma \omega_m}, \quad (9)$$

where g^m are the phonon vertices and ω_m are their frequencies. The vertices corresponding to the specific frequencies can be extracted from the EOM for the two-fermion propagators as follows:

$$g_{k_1 k_2}^m = \sum_{k_1 k_2} \widetilde{\mathcal{U}}_{k_1 k_4, k_2 k_3} \rho_{k_3 k_4}^m, \tag{10}$$

$$g_{k_1 k_2}^{m(\sigma)} = \delta_{\sigma,+1} g_{k_1 k_2}^m + \delta_{\sigma,-1} g_{k_2 k_1}^m, \tag{11}$$

where $\rho_{k_3k_4}^m$ are the matrix elements of the transition density for the mth mode of excitation of the N-particle system and $\widetilde{\mathcal{U}}_{k_1k_4,k_2k_3}$ are the matrix elements of the nucleon-nucleon interaction. As shown in Ref. [27], the relationship (10) is model independent and includes the exact transition densities, while the interaction $\widetilde{\mathcal{U}}$ is the bare interaction between nucleons in the vacuum. In practice, employing effective interactions and the random phase approximation based on these interactions for the computation of the phonon characteristics provides quite a realistic description of the dynamical self-energy. In this work, we use the effective interaction of the covariant energy density functional (CEDF) [62,63] with the NL3 parametrization [82] and the relativistic random phase approximation [83] adopted to finite temperature in our previous developments for calculations of the phonon modes [4,5,81].

The summation over ℓ' in Eq. (9) is transformed into a contour integral by the standard technique [80]. The final expression for the mass operator Σ^e , after the analytical continuation to complex energies, takes the form

$$\Sigma_{k_{1}k_{2}}^{e}(\varepsilon) = \sum_{k_{3},m} \left\{ g_{k_{1}k_{3}}^{m} g_{k_{2}k_{3}}^{m*} \frac{N(\omega_{m},T) + 1 - n(\varepsilon_{k_{3}} - \mu, T)}{\varepsilon - \varepsilon_{k_{3}} + \mu - \omega_{m} + i\delta} \right\}$$

$$+ g_{k_3k_1}^{m*} g_{k_3k_2}^m \frac{n(\varepsilon_{k_3} - \mu, T) + N(\omega_m, T)}{\varepsilon - \varepsilon_{k_3} + \mu + \omega_m - i\delta} \bigg\}, \quad (12)$$

where $\delta \to +0$, and

$$N(\omega_m, T) = \frac{1}{\exp(\omega_m/T) - 1}$$
 (13)

are the occupation numbers of phonons with frequencies ω_m , which arise from the summation over ℓ' in Eq. (9).

As in Ref. [57], in this work the self-energy (12) is treated in the diagonal approximation: $\Sigma_{k_1k_2}^e(\varepsilon) = \delta_{k_1k_2} \Sigma_{k_1}^e(\varepsilon)$. Furthermore, Eq. (8) is equivalent to the nonlinear equation

$$[\varepsilon - \varepsilon_k + \mu - \Sigma_k^e(\varepsilon)] \mathcal{G}_k(\varepsilon) = 1 \tag{14}$$

for each single-particle state k. The poles of the propagator $\mathcal{G}_k(\varepsilon)$ correspond to the zeros of the function

$$f(\varepsilon) = \varepsilon - \varepsilon_k + \mu - \Sigma_k^e(\varepsilon). \tag{15}$$

For each single-particle mean-field state k, there exist multiple solutions $\varepsilon_k^{(\lambda)}$ numbered by the additional index λ . In other words, the pole character of the energy-dependent self-energy $\Sigma_k^e(\varepsilon)$ causes fragmentation of the single-particle states k due to the PVC mechanism. The solutions $\varepsilon_k^{(\lambda)}$ can be determined by finding the zeros of $f(\varepsilon)$ or, alternatively, by the diagonalization of the arrowhead matrix [58,67]:

$$\begin{pmatrix}
\varepsilon_{k} - \mu & \xi_{n_{1}k}^{m_{1}(\sigma)} & \xi_{n_{2}k}^{m_{2}(\sigma)} & \cdots \\
\xi_{n_{1}k}^{m_{1}(\sigma)*} & \varepsilon_{n_{1}} - \mu - \sigma \omega_{m_{1}} & 0 & \cdots \\
\xi_{n_{2}k}^{m_{2}(\sigma)*} & 0 & \varepsilon_{n_{2}} - \mu - \sigma \omega_{m_{2}} & \cdots \\
\vdots & \vdots & \vdots & \ddots
\end{pmatrix},$$
(16)

where

$$\xi_{nk}^{m(\sigma)} = g_{nk}^{m(\sigma)} \sqrt{N(\omega_m, T) + n(\sigma(\varepsilon_n - \mu), T)}, \quad \sigma = \pm 1.$$
(17)

In the vicinity of the pole $\varepsilon_k^{(\lambda)}$, where the function $f(\varepsilon)$ can be approximated by

$$f(\varepsilon) \approx \left(\varepsilon - \varepsilon_k^{(\lambda)}\right) \left[1 - \frac{d}{d\varepsilon} \Sigma_k^e(\varepsilon)\right]_{\varepsilon = \varepsilon_k^{(\lambda)}},$$
 (18)

the correlated Matsubara Green function $\mathcal{G}_k(\varepsilon)$ reads

$$\mathscr{G}_{k}^{(\lambda)}(\varepsilon) \approx \frac{S_{k}^{(\lambda)}}{\varepsilon - \varepsilon_{l}^{(\lambda)}},$$
 (19)

with the spectroscopic factor

$$S_k^{(\lambda)} = \left[1 - \frac{d}{d\varepsilon} \Sigma_k^e(\varepsilon)\right]_{\varepsilon = \varepsilon_k^{(\lambda)}}^{-1}.$$
 (20)

The spectroscopic factor $S_k^{(\lambda)}$ provides a measure for the occupancy of the state λ with the single-particle quantum number

k. The spectroscopic factors $S_k^{(\lambda)}$ and the energies of the correlated states $\varepsilon_k^{(\lambda)}$ satisfy the well-known sum rules [84]

$$\sum_{\lambda} S_k^{(\lambda)} = 1, \quad \sum_{\lambda} \varepsilon_k^{(\lambda)} S_k^{(\lambda)} = \varepsilon_k, \tag{21}$$

which remain valid at finite temperature.

III. NUMERICAL SCHEME

The numerical implementation is performed in three steps. (i) The closed set of the relativistic mean-field (RMF) equations with the NL3 parametrization [82] and the thermal fermionic occupation numbers (4) is solved in a selfconsistent cycle. This procedure outputs the single-particle spectrum as a set of temperature-dependent single-particle Dirac spinors and the corresponding energies, which form the basis $\{k_i\}$ employed in further calculations. (ii) The finitetemperature RRPA (FT-RRPA) equations are solved to obtain the phonon vertices g^m and their frequencies ω_m . The FT-RRPA phonon spectrum with the RMF single (quasi)particles build the $p \otimes \text{phonon}$ and $h \otimes \text{phonon}$ configurations for the PVC self-energy $\Sigma^{e}(\varepsilon)$. (iii) Equation (8) is solved in the configuration space, truncated as described in [57]. The PVC self-energy $\Sigma^{e}(\varepsilon)$ is treated in the diagonal approximation, i.e., $\Sigma_{k_1k_2}^e(\varepsilon) = \delta_{k_1k_2}\Sigma_{k_1}^e(\varepsilon)$. Pairing correlations at T=0 are taken into account in all the three steps: in the Bardeen-Cooper-Schrieffer (BCS) approximation [34] for the mean-field calculations, in the relativistic quasiparticle RPA (RQRPA) [85] for the calculations of the phonon spectra, and in the approach of Ref. [59] for the solution of the Dyson equation. Pairing correlations were neglected in calculations at temperature $T \ge 1$ MeV as the critical temperature of the superfluid phase transition is around 1 MeV for the considered nuclei.

The particle-hole (ph) configurations with the energies $\varepsilon_{ph} \leqslant 100$ MeV and the antiparticle-hole (\$\alpha\$h) ones with $\varepsilon_{\alpha h} \geqslant -1800$ MeV, with respect to the positive-energy continuum, were included in the particle-hole basis for the FT-RRPA and RQRPA calculations of the phonon spectra. The excitation spectra converge reasonably well with this truncation, as verified by direct calculations within the complete RMF basis. The resulting vibrations with the spin-parities $J^{\pi} =$ 2^+ , 3^- , 4^+ , 5^- , 6^+ below the energy cutoff of 20 MeV formed the phonon model space. This cutoff is also justified by our previous calculations [57]. A further truncation of the phonon space was made according to the values of the reduced transition probabilities of the corresponding electromagnetic transitions B(EL). Namely, the phonon modes with B(EL)values equal to or more than 5% of the maximal one for each J^{π} were retained in the self-energy $\Sigma^{e}(\varepsilon)$. The same truncation criteria were applied for all temperature regimes. As in our previous calculations [4,5,57,81], at high temperatures many additional phonon modes appear in the excitation spectra as a consequence of the thermal unblocking, which leads to a significant expansion of the phonon model space with the temperature growth. The single-particle intermediate states k_3 were included in the summation of Eq. (12) under the condition $|\varepsilon_{k_3} - \varepsilon_{k_1}| \leq 50$ MeV. The latter implies another

TABLE I. The zero-temperature pairing gaps $\Delta_p(T=0)$ and critical temperatures T_c for even-even ^{68–76}Ni nuclei.

	⁶⁸ Ni	⁷⁰ Ni	⁷² Ni	⁷⁴ Ni	⁷⁶ Ni
$\Delta_p(T=0) \text{ (MeV)}$ $T_c \text{ (MeV)}$	1.57	1.55	1.41	1.49	1.30
	0.94	0.93	0.85	0.90	0.78

truncation of the model space, which is mild enough that the results converge. In contrast to the number of phonon modes, the number of intermediate fermionic states changes only little with temperature.

IV. RESULTS AND DISCUSSION

A. The single-(quasi)particle states: (q)PVC and temperature evolution in ^{68–78}Ni isotopic chain

The numerical implementation was performed for the chain of neutron-rich even-even Ni isotopes with atomic numbers A = 68-78, which lie on the r-process path and belong to the high-sensitivity region of the nuclear landscape with respect to the electron capture in CCSN [7–12]. We investigated the thermal evolution of the single-particle states located within the 20 MeV energy window around the respective Fermi energies of the neutron and proton subsystems. Among the selected isotopes, ⁷⁸Ni is a closed-shell nucleus as well as the proton subsystems of the other five Ni isotopes. The neutron subsystems of ^{68,70,72,74,76}Ni are open shell. As discussed in detail in Refs. [57,86], the superfluidity in the Bogoliubov or BCS sense vanishes at the critical temperature $T_c \approx$ $0.6\Delta_p(T=0)$, where $\Delta_p(T=0)$ is the pairing gap Δ_p at zero temperature. In realistic self-consistent finite-temperature calculations the coefficient between T_c and $\Delta_p(T=0)$ can be slightly different, for instance in the relativistic RMF+BCS calculations it can get close to 0.7 [57,86]. In the approaches beyond BCS the critical temperature further increases as shown, in particular, in Ref. [86]. In this work, however, we stay within the RMF+BCS description, where the critical temperature is around or below 1 MeV for the selected nuclei. Their zero-temperature neutron pairing gaps $\Delta_p(T=0)$ were determined using the three-point formula [87] and the data on the nuclear binding energies from Ref. [88]. The empirical values of the pairing gap $\Delta_p(T=0)$ and the corresponding empirical critical temperature T_c for the even-even $^{68-76}$ Ni nuclei are shown in Table I. Since our results below are presented on 1 MeV temperature grid, the pairing correlations are taken into account only at T = 0.

The reference single-particle spectra for $^{68-78}$ Ni isotopes obtained within the RMF(+BCS) approach at zero and finite temperature are shown in Figs. 1(a)-1(f). At T=0, the sizable effect of neutron pairing correlations is restricted by the neighborhood of the Fermi surface. This is reflected in the presented spectra, while the pure single-particle levels computed without pairing at T=0 are not very different from those at T=1 MeV. As a result of pairing correlations, the neutron states above (below) the Fermi surface are displaced towards higher (lower) energies. Since the chemical potential of the neutron subsystem increases with the increase of the

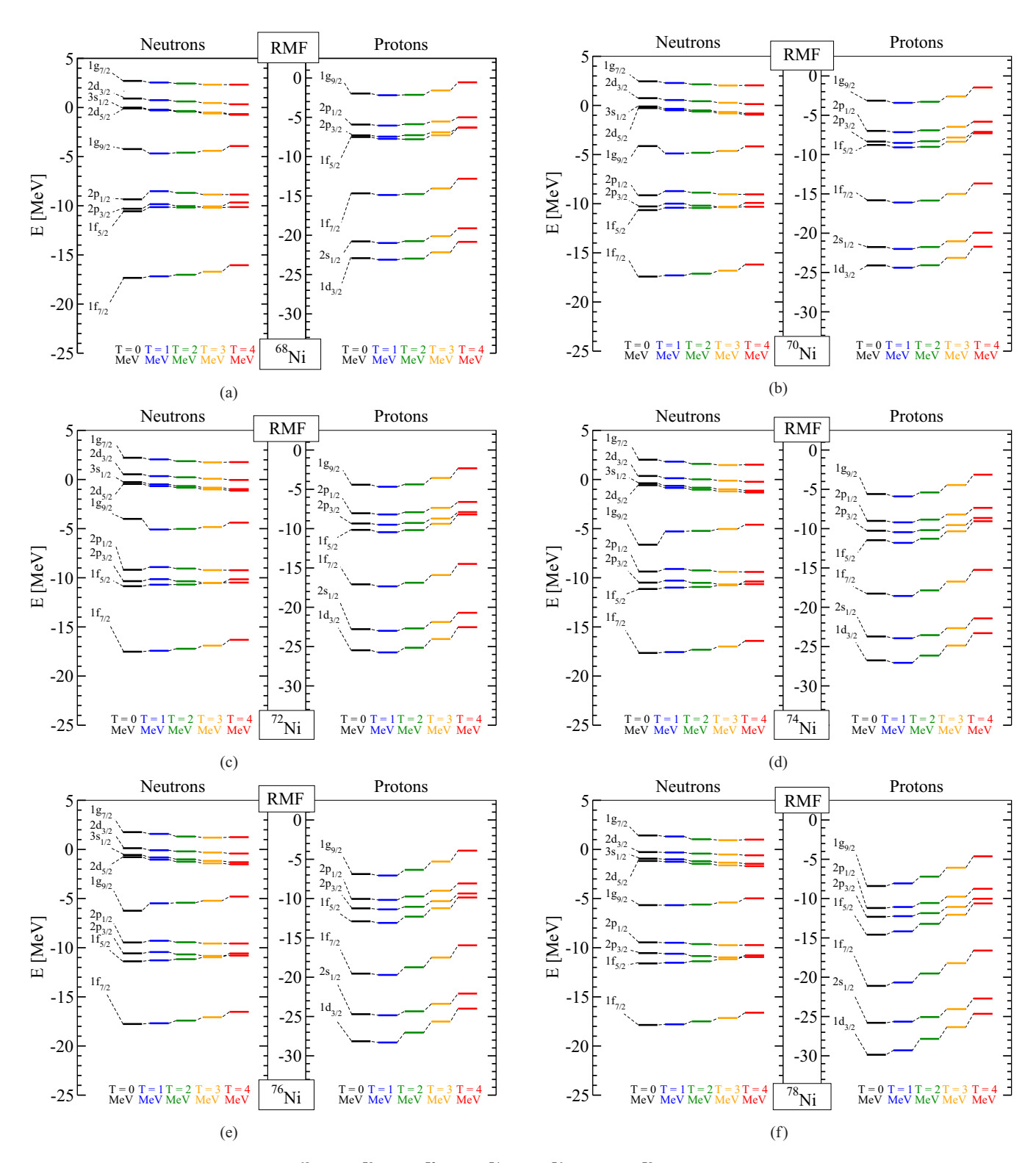


FIG. 1. Single-particle states in (a) 68 Ni, (b) 70 Ni, (c) 72 Ni, (d) 74 Ni, (e) 76 Ni, and (f) 78 Ni isotopes at zero and finite temperature calculated within the RMF approximation.

neutron number, the intruder state $1g_{9/2}$, shifted upward in $^{68-72}$ Ni isotopes, is shifted downward in 74,76 Ni isotopes. As mentioned above, superfluid pairing does not show up in the closed-shell 78 Ni and in the closed-shell proton subsystems of $^{68-76}$ Ni isotopes, although the proton states are implicitly

affected by the neutron superfluidity via the self-consistent mean field.

In general, one observes that the neutron addition induces displacements of the proton states altogether towards lower energies. As a result, the two proton shell gaps, which are

associated with the magic numbers 20 and 28, are slightly diminished with the increase of the neutron number. In the neutron subsystems of ⁶⁸⁻⁷⁶Ni isotopes, one observes an abrupt change of the neutron mean-field energies at a temperature between T = 0 and T = 1 MeV due to the superfluid phase transition at the critical temperatures T_c , given in Table I. In contrast, the doubly-magic ⁷⁸Ni nucleus shows a smooth development of the neutron mean-field energies due to the absence of the superfluid phase transition. As the temperature increases from T = 1 MeV to T = 4 MeV, the neutron mean-field states in the major shell display a tendency to densify. Analogously to the case of T = 0, at T > 0 the proton mean-field states of isotopes with larger neutron numbers also have lower energies. The overall trend of the proton meanfield energies exhibits a gradual increment of 1-2 MeV in the $1 \le T \le 4$ MeV temperature interval.

Figures 2(a)-2(f) display the dominant fragments of both neutron and proton single-particle states for ⁶⁸⁻⁷⁸Ni isotopes computed within the RMF+PVC approach. As in Refs. [57–59], we select the dominant fragment for each mean-field state according to the spectroscopic factors of the fragments. Generally, the dominant fragment is the one with the largest spectroscopic factor. In the vicinity of the Fermi energy there is typically one fragment with the spectroscopic factor of $\approx 0.7-0.9$, while the other fragments are characterized by considerably smaller spectroscopic factors (below 0.1). This fragmentation pattern is preserved at all temperatures. The neutron $1g_{9/2}$ state and the proton $1f_{7/2}$ state of ^{68–78}Ni isotopes are examples of this pattern and are called good single-particle states. The dominant fragments of these states have energies rather close to the energies of the original mean-field states. The states far away from the Fermi surface are either strongly or weakly fragmented. The strongly fragmented states are characterized by the presence of two (rarely more) competing fragments with comparable spectroscopic factors. The first fragment is chosen to be the fragment with the largest spectroscopic factor, while another fragment has a spectroscopic factor not smaller than 40% of the spectroscopic factor of the first fragment. Analogously to the good single-particle states, these two dominant fragments have energies close to their original mean-field energies. The weakly fragmented states are characterized by one fragment with a dominant spectroscopic factor, while other fragments have spectroscopic factors smaller than 40% of the spectroscopic factor of the first fragment. In this case, the dominant fragment is well defined as the one with the largest spectroscopic factor. The energy of the dominant fragment is again close to the original mean-field energy. The degree of fragmentation of a state far away from the Fermi surface can vary with temperature. One example is the neutron $2p_{3/2}$ state in ⁷⁴Ni, as displayed in Fig. 2(d). While the neutron $2p_{3/2}$ state is weakly fragmented at T = 0 and T = 3 MeV, it is strongly fragmented at T = 1 MeV, T = 2 MeV, and T = 4 MeV with 0.30/0.27, 0.17/0.33, and 0.30/0.16 shares of spectroscopic factors, respectively. The degree of fragmentation of the same state can also vary along the isotopic chain. At T = 1, the neutron $2p_{3/2}$ state is a good single-particle state in 68,70,72 Ni [see Figs. 2(a)-2(c)], whereas it is a strongly fragmented state in 74,76 Ni [see Figs. 2(d) and 2(e)]. At the same temperature, the

neutron $2p_{3/2}$ state is a weakly fragmented state in the doubly-magic ⁷⁸Ni nucleus [Fig. 2(f)]. In contrast to the neutron $2p_{3/2}$ state, which can be strongly fragmented at some temperatures, the proton $2p_{1/2}$, $1f_{5/2}$, and $2p_{3/2}$ states of ^{68–78}Ni isotopes are either good single-particle states or weakly fragmented states, as shown in the right panels of Figs. 2(a)–2(f).

For the states remote from the Fermi surface, one often encounters two or more fragments, which exhibit comparable spectroscopic factors. An example of such states is the neutron $1f_{7/2}$ state of $^{68-78}\rm{Ni}$ isotopes. The temperature evolution of this state in $^{72}\rm{Ni}$ is illustrated in Fig. 3. In general, we observe a consistent fragmentation pattern, which is preserved throughout all temperatures. For each temperature, there exists a cluster of fragments with energies lower than the mean-field energy (low-energy cluster), and another cluster with energies larger than the mean-field energy (high-energy cluster). Each cluster has one or two major fragments with relatively large spectroscopic factors. In this case, the major fragments play the role of the dominant fragments. At T=0, the dominant fragments consist of three major fragments. The low-energy fragment has the spectroscopic factor 0.20, while each of the other two fragments has the spectroscopic factor 0.13. The phase transition, which occurs around T=1MeV, together with the beginning of the thermal unblocking, modifies the strength distribution from a predominantly threepeak structure to a predominantly two-peak structure. As the temperature increases from T = 2 MeV to T = 4 MeV, the low-energy major fragment dominates, and the high-energy cluster exhibits a strong fragmentation. For comparison, the temperature evolution of the proton $2s_{1/2}$ state is illustrated in Fig. 4. Analogously to the neutron $1f_{7/2}$ state, the proton $2s_{1/2}$ state also exhibits a two-cluster structure, where the clusters are located on opposite sides of the original mean-field state. At T = 0, the dominant fragments are the two major fragments with 0.25/0.48 share of the spectroscopic factors. As the temperature increases, the low-energy cluster becomes strongly fragmented, while the high-energy major fragment in the vicinity of the Fermi energy behaves as a good singleparticle state. A similar fragmentation pattern holds for the proton $2s_{1/2}$ state in other Ni isotopes. Another example from the neutron subsystem is represented by the neutron $1g_{7/2}$ state, which is a particle state, i.e., located above the Fermi energy. In ^{68–72}Ni isotopes, this state exhibits a fragmentation pattern similar to that of the neutron $1f_{7/2}$ state in all temperature regimes, as shown in Figs. 2(a)–2(c). However, in ^{74–78}Ni isotopes, the state $1g_{7/2}$ suddenly becomes a good singleparticle state at T = 1 MeV, though it is gradually becoming more fragmented at higher temperatures [see Figs. 2(d)-2(f)].

Thereby, while the evolution of the good single-particle states in all Ni isotopes is quite similar to the evolution of the corresponding mean-field states, the evolution of the states remote from the Fermi surface exhibits various scenarios in both neutron and proton subsystems. The evolution of single-particle states in the proton subsystem remains almost unchanged across the Ni isotopic chain. In contrast, a significant modification of the fragmentation pattern occurs in the neutron subsystem. Therefore, we confine our further discussion to only the neutron single-particle states. To acquire detailed understanding of the fragmentation mechanism

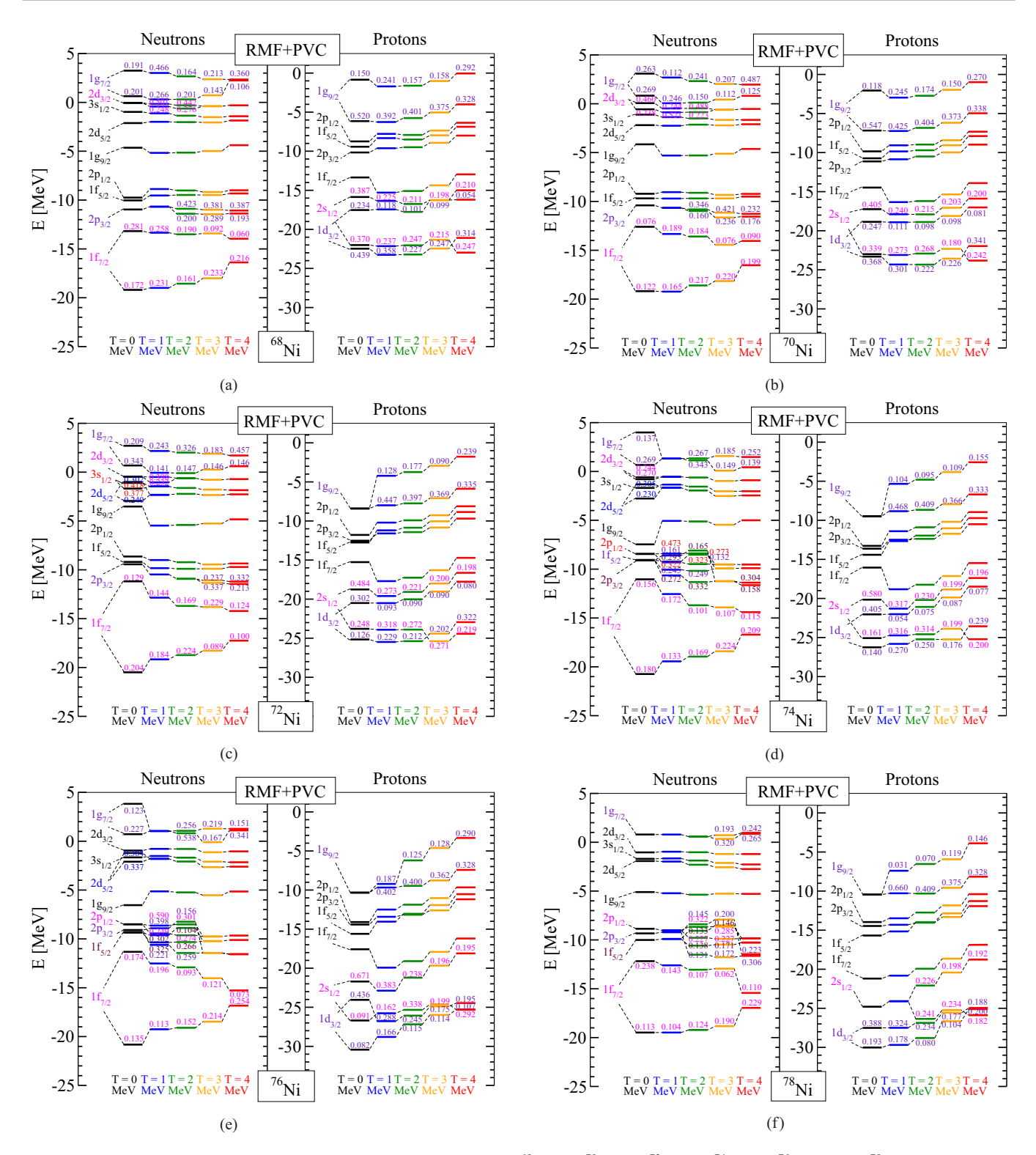


FIG. 2. The dominant fragments of the single-particle states in (a) ⁶⁸Ni, (b) ⁷⁰Ni, (c) ⁷²Ni, (d) ⁷⁴Ni, (e) ⁷⁶Ni, and (f) ⁷⁸Ni isotopes at zero and finite temperature calculated in the RMF+PVC approximation. For the strongly fragmented states, two dominant fragments are shown, and their spectroscopic factors are specified.

caused by the PVC, we examine some simplistic (toy) models of varying complexity in the Appendix. This study allows us to determine the essential factors that are responsible for the fragmentation patterns of the single-particle states at finite temperature.

Summarizing our qualitative study within the simplistic models, we particularly conclude that

(1) The number N_{λ} of fragments generated by the PVC for each phonon mode coupled to a single-particle state k

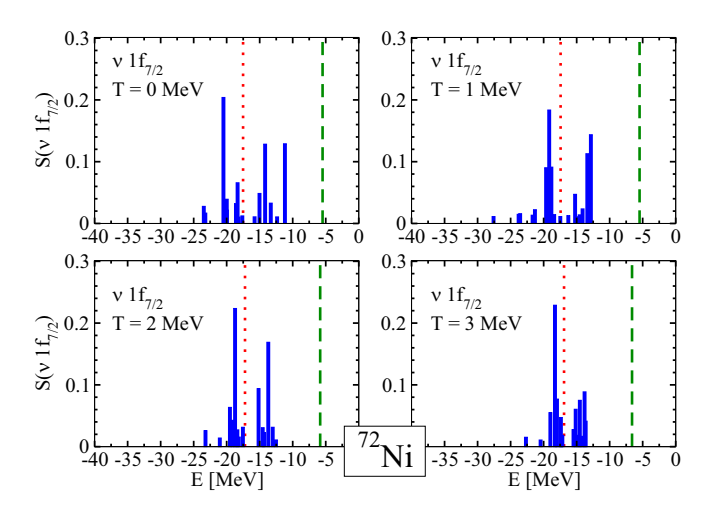


FIG. 3. Temperature evolution of the neutron $1f_{7/2}$ state of the ⁷²Ni isotope. The pure mean-field state is represented by the dotted line, while the blue bars indicate the spectroscopic factors of the fragmented states. The dashed line corresponds to the chemical potential.

satisfies the following equation:

$$N_{\lambda} = 2N_{k_3} + 1,\tag{22}$$

where N_{k_3} denotes the number of intermediate states k_3 in the mass operator Σ^e (12).

- (2) The energy differences between a specific state *k* and its neighboring states determine the degree of fragmentation of the state *k*. The state *k* is strongly fragmented if the energy differences are small.
- (3) The low-frequency phonons play the most important role in the fragmentation of the single-particle states.

B. The influence of phonons

Our qualitative study within the toy models presented in the Appendix is very instructive for understanding the general trends of the PVC mechanism; however, the toy models cannot explain the whole variety of fragmentation patterns.

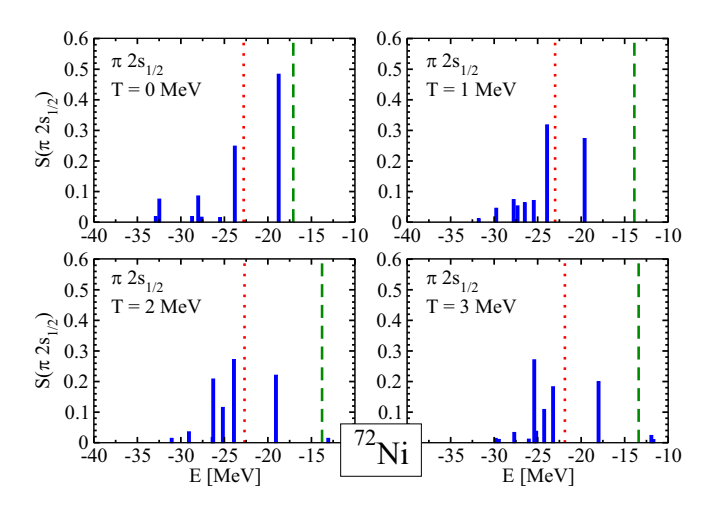


FIG. 4. Same as Fig. 3, but for the proton $2s_{1/2}$ state of the ⁷²Ni isotope.

The deficiency of the simplistic toy models is that they do not take into account the spins and parities of the mean-field states and of the various phonon modes. For example, the parity of the mean-field hole states $2p_{1/2}$, $2p_{3/2}$, $1f_{5/2}$, and $1f_{7/2}$ is negative. Consequently, the transitions between these mean-field hole states occur due to coupling to the positiveparity phonons, e.g., 2⁺ and 4⁺ phonons. Some mean-field particle states, such as $2d_{5/2}$, $3s_{1/2}$, $2d_{3/2}$, and $1g_{7/2}$, have a positive parity, whereas the states $3p_{3/2}$ and $3p_{1/2}$ lying in the continuum have a negative parity. In addition to the positive-parity phonons being responsible for the coupling between the selected particle states, the transitions between the bound and the continuum particle states originate from the coupling to the negative-parity phonons, such as the 3⁻ and 5⁻ phonons. Analogously to the bound state $1g_{7/2}$, the continuum states $3p_{3/2}$ and $3p_{1/2}$ are either weakly or strongly fragmented in ${}^{68-72}$ Ni isotopes at T>0, and suddenly become good single-particle states in ${}^{74-78}$ Ni isotopes at T=1 MeV. For a quantitative comparison, Table II shows the temperature evolution of the dominant fragments of the above mentioned continuum states in ^{70,74}Ni isotopes.

It was found in previous studies, for instance in [81,89], that the low-energy collective quadrupole 2^+ and octupole 3^- phonons couple most strongly to the single-particle degrees of freedom. This is consistent with our qualitative study discussed in the Appendix, which emphasizes the importance of the low-energy phonons for the fragmentation of single-particle states. Recall that the phonon vertices $g_{k_1k_2}^m$ are the quantitative measure of the coupling strength for the given phonon mode m, and they are related to the phonon transition densities $\rho_{k_1k_2}^m$ by Eq. (10). For each phonon mode m, at T=0 the corresponding reduced transition probability $B_m(\omega)$ reads

$$B_m(\omega) = \left| \sum_{k_1 k_2} V_{k_1 k_2}^0 \rho_{k_1 k_2}^m(\omega) \right|^2, \tag{23}$$

where V^0 is the external field, which induces an excitation from the ground to the excited state m. At the pole of the corresponding response function $\omega = \omega_m$ the reduced transition probability $B_m(\omega_m)$ is related to the strength function $S(\omega_m)$ via [90]

$$S(\omega_m) = \lim_{\Lambda \to +0} \frac{B_m(\omega_m)}{\pi \cdot \Lambda},\tag{24}$$

where Δ is the smearing parameter. From Eqs. (10), (23), and (24), one deduces that the larger the strength function $S(\omega_m)$ is at the pole, the larger are the matrix elements of the phonon vertices g^m and the stronger is the PVC. A similar correlation holds for the case of finite temperature [5,86]. Therefore, it is instructive to investigate the temperature dependence of the 2^+ and 3^- phonon low-energy strength functions. Figures 5(a)–5(f) display this dependence for the quadrupole strength distributions in $^{68-78}$ Ni. At T=1 MeV, one observes an attenuation of the low-energy 2^+ phonon strength in 70 Ni before seeing it intensifying in $^{72-78}$ Ni. In contrast, a gradual enhancement of the low-energy quadrupole phonon strengths has also been observed across the Ni isotopes at T>1 MeV. These observations correlate with the behavior of the neutron hole $2p_{1/2}$, $1f_{5/2}$, and $2p_{3/2}$ states, which

TABLE II. The temperature evolution of the dominant fragments of the continuum $3p_{1/2}$ and $3p_{3/2}$ states in 70,74 Ni isotopes. Here $\varepsilon_k^{\text{dom}}$ and S_k^{dom} represent the energy and the corresponding spectroscopic factor for each dominant fragment.

	T =	= 0	T = 1	MeV	T=2	MeV	T=3	MeV	T=4	MeV
	$rac{arepsilon_k^{ m dom}}{({ m MeV})}$	$S_k^{ m dom}$	$rac{arepsilon_k^{ m dom}}{ m (MeV)}$	$S_k^{ m dom}$	$\varepsilon_k^{ m dom} \ ({ m MeV})$	$S_k^{ m dom}$	$\varepsilon_k^{ m dom} \ m (MeV)$	$S_k^{ m dom}$		
⁷⁰ Ni										
$3p_{1/2}$	3.226	0.918	2.889	0.303	2.836	0.317	2.681	0.342	2.583	0.643
1 -/-			3.204	0.673	3.162	0.514	3.055	0.505	3.021	0.285
$3p_{3/2}$	3.119	0.954	2.766	0.534	2.795	0.565	2.677	0.587	2.491	0.866
,			3.054	0.333	3.110	0.286				
⁷⁴ Ni										
$3p_{1/2}$	3.082	0.348	2.992	0.885	2.948	0.245	2.750	0.386	2.213	0.379
1 -/-	3.106	0.602			3.053	0.536	2.938	0.186	2.689	0.569
$3p_{3/2}$	2.979	0.950	2.884	0.967	2.624	0.292	2.538	0.348	2.209	0.622
,					2.825	0.662	2.707	0.175	2.508	0.279

are strongly fragmented in 74,76 Ni isotopes, whereas they are good single-particle states in $^{68-72}$ Ni isotopes, as follows from Figs. 2(a)–2(e). The temperature dependence of the octupole strength distributions across the Ni isotopes is again different, as shown in Figs. 6(a)–6(f). At T=1 MeV, one observes a slow but steady attenuation of the low-lying phonon strengths throughout the Ni isotopes. At other temperatures, one observes rather a steady increase of the low-lying 3^- phonon strength. The attenuation of the low-lying phonon strengths at T=1 MeV is responsible, for instance, for the change

of the fragmentation pattern of the particle bound state $1g_{7/2}$ and of the continuum states $3p_{1/2}$ and $3p_{3/2}$, which transition from being fragmented states in $^{68-72}$ Ni to becoming good single-particle states in $^{74-78}$ Ni.

C. Temperature dependence of the nucleon effective mass and symmetry energy

The nucleon effective mass is a very important characteristic of nuclear matter and finite nuclei. On the microscopic

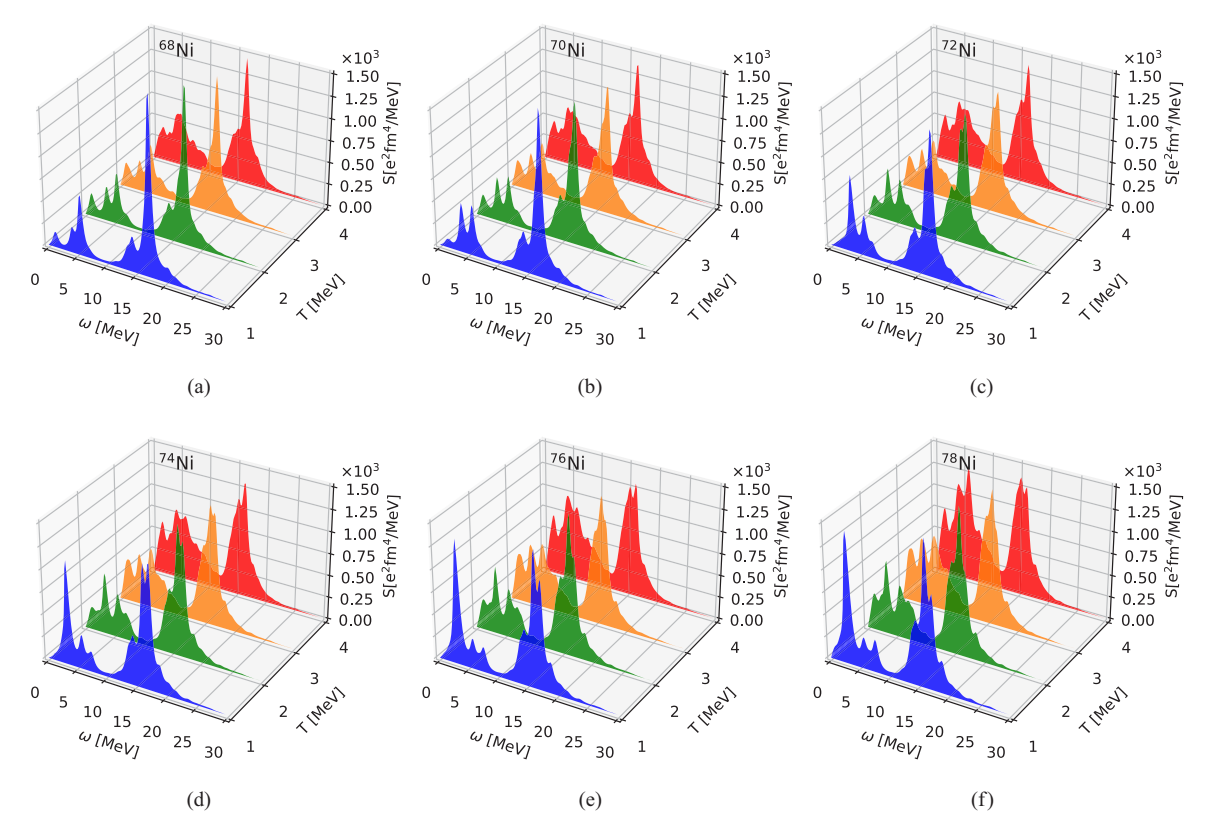


FIG. 5. Temperature dependence of the quadrupole (2^+) phonon strength distributions in (a) 68 Ni, (b) 70 Ni, (c) 72 Ni, (d) 74 Ni, (e) 76 Ni, and (f) 78 Ni.

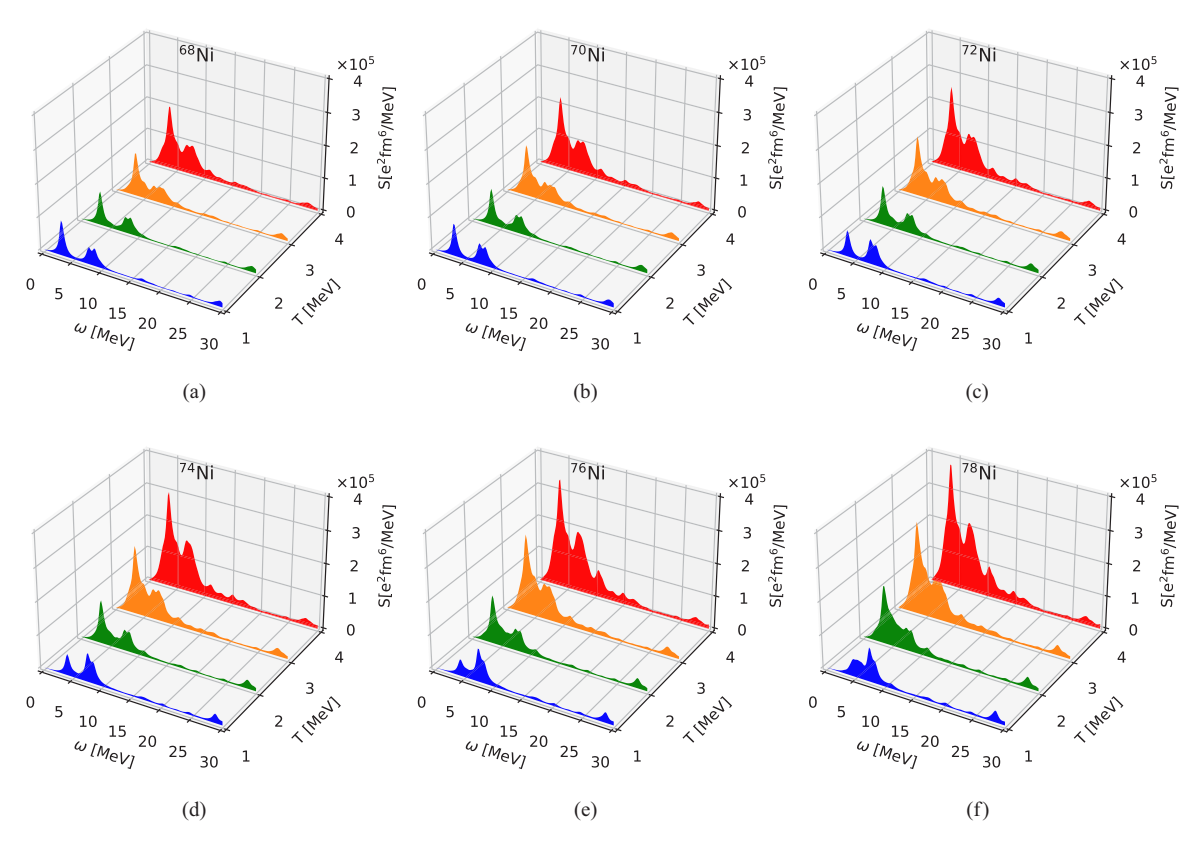


FIG. 6. Temperature dependence of the octupole (3⁻) phonon strength distributions in (a) ⁶⁸Ni, (b) ⁷⁰Ni, (c) ⁷²Ni, (d) ⁷⁴Ni, (e) ⁷⁶Ni, and (f) ⁷⁸Ni.

level, it accounts for all effects of the strongly interacting medium on a single nucleon via the self-energy, the dynamical (energy-dependent) part of which is modeled by Eq. (9). The static part of the self-energy is conventionally included in the mean-field propagator (1), and it is associated with the k mass [71,91,92]. The resulting effective mass peaks at the Fermi surface, due to the pole structure of the dynamical self-energy [71,91]. This functional dependence survives at finite temperature, although its sharpness decreases with the temperature growth [15,57]. Furthermore, the temperature dependence of the nuclear symmetry energy, a key ingredient of the nuclear equation of state (EOS), can be established via the temperature-dependent nucleon effective mass [14-16].

The temperature-dependent nucleon effective mass m^* is defined as [14,16]

$$\frac{m^*(T)}{M} = \frac{\widetilde{m}}{M} \frac{m_{\omega}(T)}{M},\tag{25}$$

where M, \widetilde{m} , and $m_{\omega}(T)$ are the bare nucleon mass, k mass, and ω mass, respectively. The k mass only weakly depends on temperature, so that its value is mostly defined by the parametrization being used. For the NL3 parametrization, the value of k mass is 0.60M [82]. To determine the value of $m_{\omega}(T)$ for each temperature T, we first define the quantity $\overline{m}_{(k)}(E,T)$ for each single-particle state $k=\{(k),m_k\}$ as

$$\frac{\overline{m}_{(k)}(E,T)}{M} = 1 - \frac{\partial}{\partial \varepsilon} \operatorname{Re} \Sigma_{(k)}^{e}(\varepsilon), \tag{26}$$

where the energy argument ε is a complex variable, i.e., $\varepsilon = E + i\Delta$, the indices in the brackets stand for the reduced matrix elements, and m_k denotes the magnetic quantum numbers. As in the effective mass calculations, we should target the vicinity of the Fermi surface, in the calculations discussed below the real part E has the range $|E - \mu| \le 5$ MeV. The imaginary part Δ can be chosen as the averaged distance between the energy fragments with spectroscopic factors larger than 0.5 within the given interval of E values. The temperature-dependent ω mass $m_{\omega}(T)$ is then associated with the maximal value of the average $\overline{m}_{(k)}(E,T)/M$ over the single-particle states k, viz.,

$$\frac{m_{\omega}(T)}{M} = \max_{E} \left[\frac{\sum_{(k)} (2j_{(k)} + 1)\overline{m}_{(k)}(E, T)/M}{\sum_{(k)} (2j_{(k)} + 1)} \right]. \tag{27}$$

Following Ref. [14], the temperature dependence of the ω mass can be parametrized as follows:

$$\frac{m_{\omega}(T)}{M} = 1 + \left[\frac{m_{\omega}(T=0)}{M} - 1 \right] e^{-T/T_0}, \tag{28}$$

where $m_{\omega}(T=0)/M$ and T_0 are fitting parameters.

Furthermore, the impact of the temperature dependence of the ω mass on the symmetry energy can be determined. In the nuclear EOS, the symmetry energy term reads

$$E_S = S(T=0) \left(1 - 2\frac{Z}{A}\right)^2,$$
 (29)

TABLE III. Best values of parameters $m_{\omega}(T=0)/M$ and T_0 for the exponential fit (28).

	⁶⁸ Ni	⁷⁰ Ni	⁷² Ni	⁷⁴ Ni	⁷⁶ Ni	⁷⁸ Ni
$m_{\omega}(T=0)/M$	1.33	1.34	1.39	1.54	1.34	1.14
$T_0 \text{ (MeV)}$	1.59	1.99	1.61	0.96	1.26	4.80

where S(T=0) is the symmetry coefficient of the nuclear matter at zero temperature. For the NL3 parametrization, S(T=0)=37.4 MeV. It should be noted that this value implicitly contains the contribution from the particle-vibration coupling and pairing effects at zero temperature, because the parameters of the NL3 meson-nucleon Lagrangian were obtained by fitting nuclear masses and radii on the mean-field level [82]. One can, thus, estimate the contribution of the PVC and pairing correlations at finite temperature using the Fermi gas model. According to this model, the contribution from the PVC and pairing effects (qPVC) at temperature T contains two parts, i.e., the kinetic part which scales as $1/m^*(T)$ and the temperature-independent potential V:

$$E_{qPVC}(T) = \frac{\hbar^2 c^2 k_F^2}{6M} \left[\frac{M}{m^*(T)} \right] + V.$$
 (30)

Therefore, the symmetry coefficient S(T) at finite temperature reads

$$S(T) = S(T=0) + \frac{\hbar^2 c^2 k_F^2}{6M} \left[\frac{M}{m^*(T)} - \frac{M}{m^*(T=0)} \right],$$
(31)

where the subtraction of the PVC and pairing contributions at T = 0 aims to overcome double counting. To complete the calculation scheme, we use the expression for the Fermi momentum k_F via the nuclear matter density ρ_0 :

$$k_F = \left(\frac{3}{2}\pi^2 \rho_0\right)^{1/3}. (32)$$

For the NL3 parametrization, $\rho_0 = 0.148 \text{ fm}^{-3}$ and, thus, $k_F = 1.30 \text{ fm}^{-1}$. For each temperature T, the effective mass $m^*(T)$ was calculated using Eq. (25), where the value of $m_\omega(T)/M$ was obtained from Eq. (28). By performing the fitting of our microscopically computed ω mass, we found the best values of these parameters for ^{68–76}Ni isotopes. They are summarized in Table III for the $0 \le T \le 2$ MeV temperature interval, which is the most relevant range of temperatures in astrophysical modeling, such as CCSN simulations [15]. Although these parameters are apparently model dependent, they are in a reasonable agreement with those obtained in the semiphenomenological calculations of Ref. [14].

The best values of $m_{\omega}(T=0)$ and T_0 were obtained as the averaged values of these two parameters over the five Ni isotopes under study: $m_{\omega}(T=0)/M=1.39$ and $T_0=1.48$ MeV. The resulting values of the effective mass $m^*(T)$ and the symmetry coefficient S(T) for the $0 \le T \le 2$ MeV temperature interval are summarized in Table IV. They illustrate a remarkable increase of the symmetry coefficient with temperature T, while the effective mass decreases considerably. Figure 7

TABLE IV. The temperature evolution of the effective mass $m^*(T)/M$ and symmetry coefficient S(T).

	T = 0 $T =$		T = 1.5 MeV	T = 2.0 MeV		
m^*/M	0.83	0.72	0.68	0.66		
S (MeV)	37.4	39.6	40.4	41.1		

displays the evolution of the symmetry coefficient S(T) with temperature in Ni isotopes associated with the asymmetry parameter δ^2 , where $\delta = (N-Z)/A$, for $0 \le T \le 2$ MeV. One can see in Fig. 7 that, in particular, at all temperatures (i) the symmetry coefficient peaks at ⁷⁴Ni, and (ii) the doubly magic nucleus ⁷⁸Ni has the lowest symmetry coefficient. This trend can be explained by Eq. (31), which indicates that the larger effective mass $m^*(T=0)$ at zero temperature leads to a larger symmetry coefficient S(T). Meanwhile, since the k mass is constant, the trend of the effective mass $m^*(T=0)$ throughout the Ni isotopic chain is solely governed by the ω mass.

The temperature and energy dependencies of the ω mass were analyzed in detail in Ref. [57] for the cases of ^{56,68}Ni, and we refer the interested reader to this recent work for a more complete picture of these dependencies. In the present study we focused on the peak value of the ω mass, which is largely determined by $\bar{m}_{(k)}(E_m, T)$, where E_m is the energy of the peak. It is typically very close to the Fermi energy. As follows from Eq. (26), the mass $\bar{m}_{(k)}(E_m, T)$ is inversely proportional to the spectroscopic factor of the state k as a function of energy and, furthermore, in the presence of pairing correlations, to the occupation numbers $(v_{(k)}^2)$ in the BCS approximation) of the single-quasiparticle states around the Fermi level. This explains why the symmetry energy coefficient is maximal in ⁷⁴Ni, if we compare the spectroscopic factors of the dominant fragments around the Fermi surface and the corresponding BCS occupation probabilities. Table V summarizes the spectroscopic factors of the dominant fragments around the Fermi surface for the considered nickel

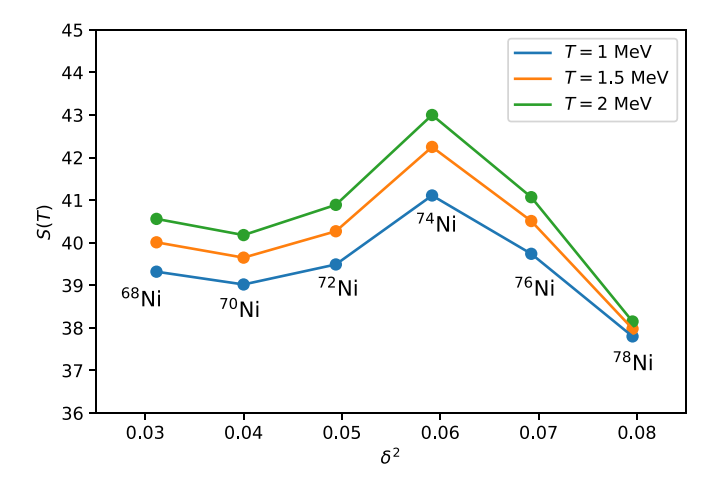


FIG. 7. The dependence of the symmetry coefficient S(T) on the asymmetry parameter δ^2 for T=1 MeV, T=1.5 MeV, and T=2 MeV (lower, middle and upper symbols, respectively).

TABLE V. The dominant spectroscopic factors for the good single-quasiparticle states around the Fermi surface (strongly fragmented states not shown).

Nucleus	$2d_{5/2}$	$2d_{3/2}$	$3s_{1/2}$	$1g_{9/2}$	$2p_{1/2}$	$2p_{3/2}$	$1f_{5/2}$
⁶⁸ Ni				0.812	0.839	0.765	0.790
⁷⁰ Ni	0.540			0.808	0.824	0.676	0.756
⁷² Ni				0.730	0.733	0.522	0.617
⁷⁴ Ni			0.653	0.752	0.708	0.537	0.580
⁷⁶ Ni		0.597	0.755	0.655	0.752	0.608	0.605
⁷⁸ Ni	0.884		0.892	0.800	0.852	0.709	0.708

isotopes. One can see immediately that the mid-subshell isotopes $^{72-76}\rm{Ni}$ exhibit the lower spectroscopic factors, or stronger fragmentation, as compared to those forming the closed subshell ($^{68}\rm{Ni}$) and closed shell ($^{78}\rm{Ni}$). Moreover, $^{74}\rm{Ni}$ has the lowest value of the BCS occupation probability $v_{(k)}^2=0.53$ for the $1g_{9/2}$ state, which makes the dominant contribution at the Fermi surface, that further enhances the neutron effective mass in $^{74}\rm{Ni}$ at T=0, where the superfluid pairing vanishes. This explains the maximum of the symmetry energy coefficient in $^{74}\rm{Ni}$.

V. SUMMARY AND OUTLOOK

In this work, we investigated fragmentation patterns of the single-particle states in neutron-rich nuclei at finite temperature. The Dyson equation for the fermionic propagator with an energy-dependent mass operator, or dynamical self-energy. including the PVC mechanism was solved numerically in the basis of the thermal relativistic mean field for the even-even neutron-rich nickel isotopes with atomic masses A = 68-78. As in the zero-temperature case, the dynamical self-energy at finite temperature is responsible for the fragmentation of the mean-field single-particle states, while finite temperature represents another dimension in the model parameter space to reveal the microscopic aspects of the particle-vibration coupling. Complete fragmented single-particle spectra in the 20 MeV window around the Fermi energies of the considered nuclei were extracted, and their temperature evolution was analyzed.

Furthermore, the temperature-dependent nucleon effective mass $m^*(T)$ was extracted from the calculated spectra of nickel isotopes. Being itself a very important quantity defining the nuclear EOS with significant consequences for the CCSN [76], the nucleon effective mass is related to the symmetry energy, whose temperature dependence can be deduced from $m^*(T)$. We found that the symmetry energy coefficient S(T)grows with temperature, in agreement with earlier studies [14,77]; however, the concrete values of this coefficient found in this work follow from more advanced microscopic calculations. In particular, an isotopic dependence of S(T) was accurately determined for the neutron-rich nickel isotopes, which represent a high-sensitivity region of the nuclear landscape for the r process and CCSN. An enhancement of the symmetry energy coefficient was found in the mid-subshell isotopes that is linked to the enhancement of the superfluid

pairing correlations below the critical temperature as well as the PVC effects in those nuclear systems.

To investigate the essential factors determining the fragmentation patterns of single-particle states, we examined toy systems consisting of one, two, and three single-particle states and one phonon. We found that the fragmentation is sensitive to such quantities as the phonon frequency, the PVC coupling strength, and the distance between the single-particle states. The sensitivity of the single-particle spectroscopic factors and fragment energies to these characteristics is quantified by varying them independently at various values of temperature. These studies explain the fragmentation patterns obtained in realistic calculations; in particular, we established how the temperature evolution of the phonon modes translates to the evolution of the fragmentation patterns via the PVC mechanism.

The systematic studies presented in this work further advance the understanding of the behavior of atomic nuclei at extremal conditions. Here we investigated the extremes of isospin and temperature, which are of prime importance for astrophysical modeling of cataclysmic events, such as neutron star mergers and supernova explosions. The nuclear single-particle properties in the astrophysical environments underly the behavior of the reaction rates, such as neutron capture, beta decay, and electron capture, which are pivotal for modeling r-process nucleosynthesis and the core collapse of the supernovae. These rates require calculations of fermionic two-body propagators in correlated media in a similar manner [6,13], while the results obtained in this work can be directly used for studying the evolution of nuclear level densities with temperature, which are another important part of the nuclear physics input for the astrophysical modeling. Such studies will be addressed by future efforts.

ACKNOWLEDGMENTS

This work is partly supported by the US-NSF Career Grant No. PHY-1654379 and US-NSF Grant No. PHY-2209376.

APPENDIX: TOY MODELS

1. One-level model

Let us first consider a system which consists of one state k_1 and one phonon with frequency ω_1 . Under these conditions, Eq. (12) for the diagonal mass operator $\Sigma_{k_1}^{\varepsilon}(\varepsilon)$ takes the form

$$\begin{split} \Sigma_{k_1}^e(\varepsilon) &= g_{k_1 k_1}^{1*} g_{k_1 k_1}^1 \left\{ \frac{N(\omega_1, T) + 1 - n(\varepsilon_{k_1} - \mu, T)}{\varepsilon - \varepsilon_{k_1} + \mu - \omega_1} \right. \\ &+ \frac{n(\varepsilon_{k_1} - \mu, T) + N(\omega_1, T)}{\varepsilon - \varepsilon_{k_1} + \mu + \omega_1} \right\}. \end{split} \tag{A1}$$

The diagonalization of the matrix

$$\begin{pmatrix} \varepsilon_{k_1} - \mu & \xi_{k_1 k_1}^{1(+1)} & \xi_{k_1 k_1}^{1(-1)} \\ \xi_{k_1 k_1}^{1(+1)*} & \varepsilon_{k_1} - \mu - \omega_1 & 0 \\ \xi_{k_1 k_1}^{1(-1)*} & 0 & \varepsilon_{k_1} - \mu + \omega_1 \end{pmatrix}, \quad (A2)$$

where

$$\xi_{k_1 k_1}^{1(\pm 1)} = g_{k_1 k_1}^{1(\pm 1)} \sqrt{N(\omega_1, T) + n(\pm (\varepsilon_{k_1} - \mu), T)}, \quad (A3)$$

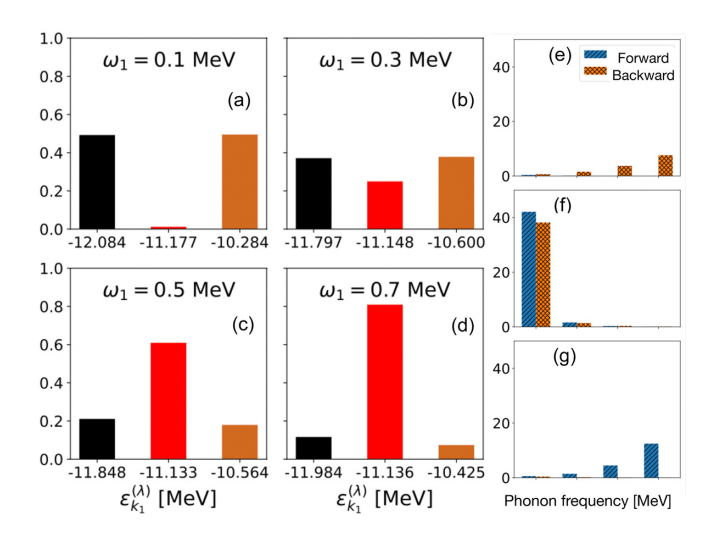


FIG. 8. (a)–(d) The evolution of spectroscopic factors $S_{k_1}^{(\lambda)}$ for the state $1f_{7/2}$ with the phonon frequency ω_1 at T=1 MeV. The left, middle, and right bars correspond to $\varepsilon_{k_1}^{(1)}$, $\varepsilon_{k_1}^{(2)}$, and $\varepsilon_{k_1}^{(3)}$, respectively. (e)–(g) Contributions (in %) from the forward and backward going terms of the spectroscopic factors $S_{k_1}^{(1,2,3)}$ for the fragment energies $\varepsilon_{k_1}^{(1)}$ (e), $\varepsilon_{k_1}^{(2)}$ (f), and $\varepsilon_{k_1}^{(3)}$ (g).

results in three different energies $\varepsilon_{k_1}^{(\lambda)}$ ($\lambda=1,2,3$). For each λ , the corresponding spectroscopic factor $S_{k_1}^{(\lambda)}$ reads

$$S_{k_{1}}^{(\lambda)} = \left\{ 1 + g_{k_{1}k_{1}}^{1*} g_{k_{1}k_{1}}^{1} \left[\frac{N(\omega_{1}, T) + 1 - n(\varepsilon_{k_{1}} - \mu, T)}{[\varepsilon - \varepsilon_{k_{1}} + \mu - \omega_{1}]^{2}} + \frac{n(\varepsilon_{k_{1}} - \mu, T) + N(\omega_{1}, T)}{[\varepsilon - \varepsilon_{k_{1}} + \mu + \omega_{1}]^{2}} \right\}_{\varepsilon = \varepsilon_{k_{1}}^{(\lambda)}}^{-1}.$$
(A4)

In contrast to the case of zero temperature, both forward going and backward going terms (the first and second terms in the square brackets) take nonvanishing values for the same mean-field reference state k_1 , regardless of its location. This occurs because of the smooth Fermi and Bose distribution functions in the numerators, and makes the fragmentation pattern different from the one at zero temperature.

To illustrate this model, we computed the spectroscopic factors $S_{k_1}^{(\lambda)}$ for the specific neutron state $1f_{7/2}$ of ⁷⁰Ni at fixed temperature T = 1 MeV. From the thermal RMF calculations, the RMF energy ε_{k_1} of the state $1f_{7/2}$ and the chemical potential μ at T=1 MeV are obtained as -17.296MeV and -6.114 MeV, respectively. The phonon vertex $g_{k_1k_1}^1$ is taken equal to 0.2 MeV, which is a typical value for the major phonon vertices calculated within FT-RRPA. Figures 8(a)-8(d) demonstrate the evolution of the spectroscopic factors $S_{k_1}^{(\lambda)}$ with the phonon frequency ω_1 . As one can see, both first and third energy fragments are dominant at $\omega_1 \leq 0.3$ MeV, while the second fragment becomes the dominant state at $\omega_1 > 0.3$ MeV. The critical phonon frequency $\omega_1^{\rm crit} \approx 0.3$ MeV refers to the phonon frequency where the second fragment starts becoming dominant and the number of competing fragments is maximal, i.e., equal to 3. A large number of competing fragments can be associated with strong

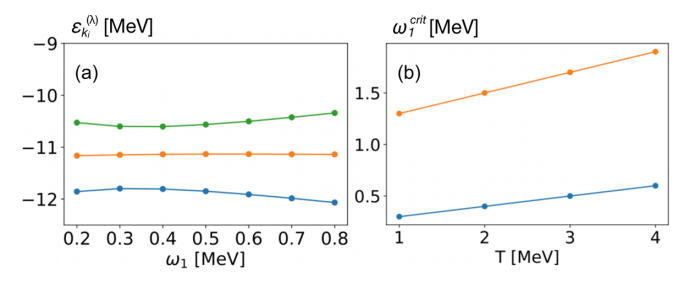


FIG. 9. The evolution of the fragment energies $\varepsilon_{k_1}^{(\lambda)}$ with the phonon frequency ω_1 at T=1 MeV (a) and the evolution of the critical phonon frequency $\omega_1^{\rm crit}$ with temperature T for $g_{k_1k_1}^1=0.2$ (upper line) and $g_{k_1k_1}^1=2.0$ (lower line) (b).

PVC. Moreover, as shown in Fig. 9(a), the energy differences $\varepsilon_{k_1}^{(2)} - \varepsilon_{k_1}^{(1)}$ and $\varepsilon_{k_1}^{(3)} - \varepsilon_{k_1}^{(2)}$ between the fragmented states are minimal at $\omega_1 = \omega_1^{\text{crit}}$. This implies a correlation between the proximity of the fragments to each other and the degree of fragmentation. Equation (A4) suggests that the evolution of the spectroscopic factors $S_{k_1}^{(\lambda)}$ with the phonon frequency ω_1 is determined by the interplay between the forward going and backward going terms. To better understand this interplay, we track the evolution of the forward going and backward going terms with the phonon frequency ω_1 for each energy fragment $\varepsilon_{k_1}^{(\lambda)}$, as displayed in Figs. 8(e)-8(g). As can be seen in Fig. 8(f), there is an almost equal contribution of the forward and backward going terms to the spectroscopic factor $S_k^{(2)}$ for all the phonon frequencies ω_1 , while the backward (forward) going term is always dominant in the first (third) energy fragment, as shown in Fig. 8(e) [8(g)]. At $\omega_1 < 0.3$ MeV, the total contribution of the forward and the backward going terms to the second energy fragment is larger than to the other two fragments, leading to the larger spectroscopic factors. Starting from $\omega_1^{\rm crit} \approx 0.3$ MeV, a rapid growth of the backward (forward) going terms in the inverse spectroscopic factor $S_{k_1}^{(1)}$ $(S_{k_1}^{(3)})$ occurs, that is associated with a quick decrease of the spectroscopic factor $S_{k_1}^{(2)}$ of the second fragment. Similar trends are observed for different temperatures T and different values of the phonon vertex $g_{k_1k_1}^1$. For a fixed phonon vertex $g_{k_1k_1}^1 = 0.2$ MeV, one observes an increase of the critical phonon frequency ω_1^{crit} by the amount of roughly 0.1 MeV per 1 MeV temperature step. However, a somewhat faster increase of ω_1^{crit} is recorded when one increases the value of $g_{k_1k_1}^1$ by one order of magnitude, as seen in Fig. 9(b). Thus, the first toy model demonstrates how the evolution of the spectroscopic factors $S_{k_1}^{(\lambda)}$ with temperature T is governed by the phonon frequency ω_1 and the magnitude of the phonon vertex $g_{k_1k_1}^1$.

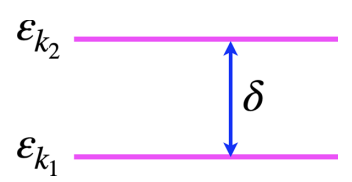


FIG. 10. The two states k_1 and k_2 with the energy difference δ in the second toy model.

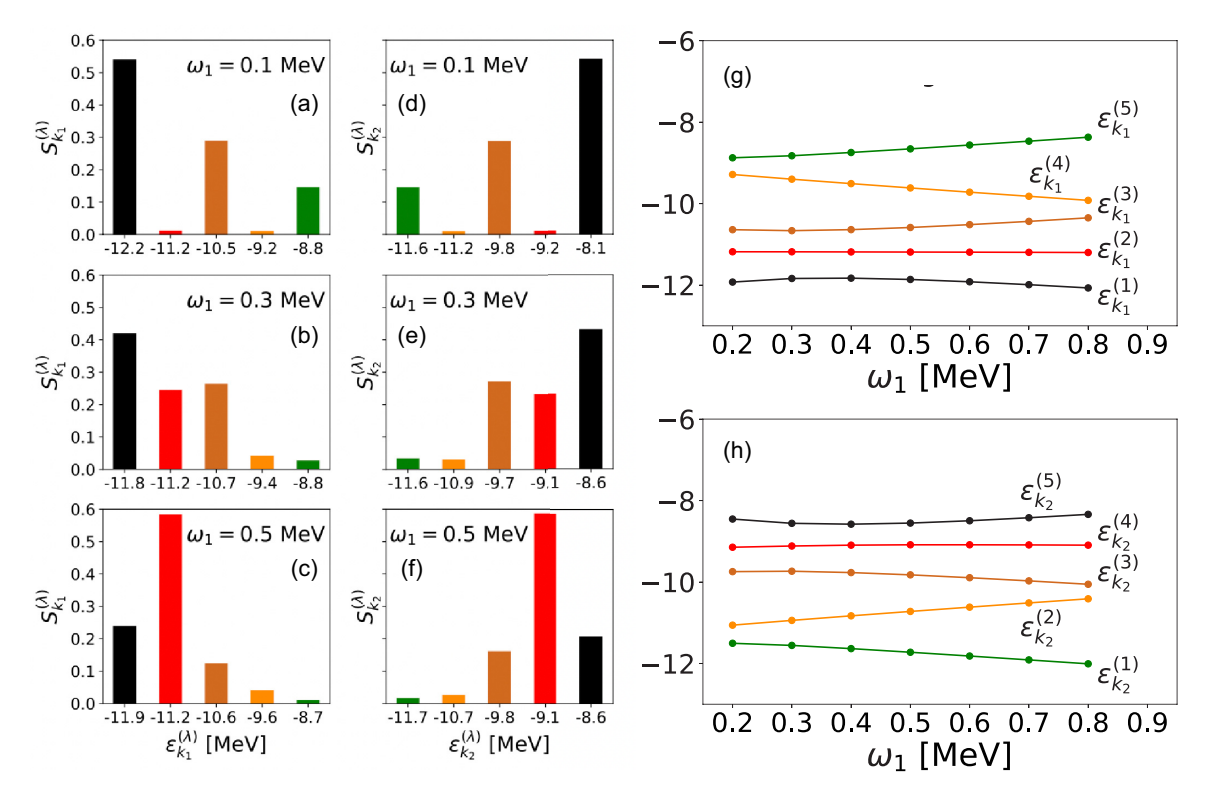


FIG. 11. The evolution of the spectroscopic factors $S_{k_1}^{(\lambda)}$ (a)–(c) and $S_{k_2}^{(\lambda)}$ (d)–(f), and the fragment energies $\varepsilon_{k_1}^{(\lambda)}$ (g) and $\varepsilon_{k_2}^{(\lambda)}$ (h) with the phonon frequency ω_1 at T=1 MeV and $\delta=2.0$ MeV.

2. Two-level model

In the second toy model, we add another state k_2 to the previous state k_1 with the energy difference $\delta \equiv \varepsilon_{k_2} - \varepsilon_{k_1} > 0$, as shown in Fig. 10. For the case of a two-level system with one phonon mode, the two diagonal mass operators $\Sigma_{k_1}^e(\varepsilon)$ and $\Sigma_{k_2}^e(\varepsilon)$, respectively, take the forms

$$\Sigma_{k_{1}}^{e}(\varepsilon) = g_{k_{1}k_{1}}^{1} g_{k_{1}k_{1}}^{1*} \frac{N(\omega_{1}, T) + 1 - n(\varepsilon_{k_{1}} - \mu, T)}{\varepsilon - \varepsilon_{k_{1}} + \mu - \omega_{1}}$$

$$+ g_{k_{1}k_{1}}^{1*} g_{k_{1}k_{1}}^{1} \frac{n(\varepsilon_{k_{1}} - \mu, T) + N(\omega_{1}, T)}{\varepsilon - \varepsilon_{k_{1}} + \mu + \omega_{1}}$$

$$+ g_{k_{1}k_{2}}^{1} g_{k_{1}k_{2}}^{1*} \frac{N(\omega_{1}, T) + 1 - n(\varepsilon_{k_{2}} - \mu, T)}{\varepsilon - \varepsilon_{k_{2}} + \mu - \omega_{1}}$$

$$+ g_{k_{2}k_{1}}^{1*} g_{k_{2}k_{1}}^{1} \frac{n(\varepsilon_{k_{2}} - \mu, T) + N(\omega_{1}, T)}{\varepsilon - \varepsilon_{k_{2}} + \mu + \omega_{1}}$$
(A5)

and

$$\Sigma_{k_{2}}^{e}(\varepsilon) = g_{k_{2}k_{1}}^{1} g_{k_{2}k_{1}}^{1*} \frac{N(\omega_{1}, T) + 1 - n(\varepsilon_{k_{1}} - \mu, T)}{\varepsilon - \varepsilon_{k_{1}} + \mu - \omega_{1}}$$

$$+ g_{k_{1}k_{2}}^{1*} g_{k_{1}k_{2}}^{1} \frac{n(\varepsilon_{k_{1}} - \mu, T) + N(\omega_{1}, T)}{\varepsilon - \varepsilon_{k_{1}} + \mu + \omega_{1}}$$

$$+ g_{k_{2}k_{2}}^{1} g_{k_{2}k_{2}}^{1*} \frac{N(\omega_{1}, T) + 1 - n(\varepsilon_{k_{2}} - \mu, T)}{\varepsilon - \varepsilon_{k_{2}} + \mu - \omega_{1}}$$

$$+ g_{k_{2}k_{2}}^{1*} g_{k_{2}k_{2}}^{1} \frac{n(\varepsilon_{k_{2}} - \mu, T) + N(\omega_{1}, T)}{\varepsilon - \varepsilon_{k_{2}} + \mu + \omega_{1}}.$$
 (A6)

The solutions $\varepsilon_{k_1}^{(\lambda)}$ and $\varepsilon_{k_2}^{(\lambda)}$, where $\lambda = 1, 2, ..., 5$, are obtained by diagonalizing the following two matrices:

$$\begin{pmatrix}
\varepsilon_{k_{1}} - \mu & \xi_{k_{1}k_{1}}^{1(+1)} & \cdots & \ddots & \xi_{k_{2}k_{1}}^{1(-1)} \\
\xi_{k_{1}k_{1}}^{1(+1)*} & \varepsilon_{k_{1}} - \mu - \omega_{1} & 0 & \cdots & 0 \\
\vdots & 0 & \ddots & \cdots & 0 \\
\vdots & \vdots & \vdots & \ddots & 0 \\
\xi_{k_{2}k_{1}}^{1(-1)*} & 0 & 0 & 0 & \varepsilon_{k_{2}} - \mu + \omega_{1}
\end{pmatrix}$$
(A7)

and

$$\begin{pmatrix} \varepsilon_{k_{2}} - \mu & \xi_{k_{1}k_{2}}^{1(+1)} & \cdots & \cdots & \xi_{k_{2}k_{2}}^{1(-1)} \\ \xi_{k_{1}k_{2}}^{1(+1)*} & \varepsilon_{k_{1}} - \mu - \omega_{1} & 0 & \cdots & 0 \\ \vdots & 0 & \ddots & \cdots & 0 \\ \vdots & \vdots & \vdots & \ddots & 0 \\ \xi_{k_{2}k_{2}}^{1(-1)*} & 0 & 0 & 0 & \varepsilon_{k_{2}} - \mu + \omega_{1} \end{pmatrix}.$$
(A8)

According to Eq. (20), the corresponding spectroscopic factors $S_{k_1}^{(\lambda)}$ and $S_{k_2}^{(\lambda)}$ are determined via

$$S_{k_i}^{(\lambda)} = \left[1 - \frac{d}{d\varepsilon} \Sigma_{k_i}^e(\varepsilon)\right]_{\varepsilon = \varepsilon_{k_i}^{(\lambda)}}^{-1}.$$
 (A9)

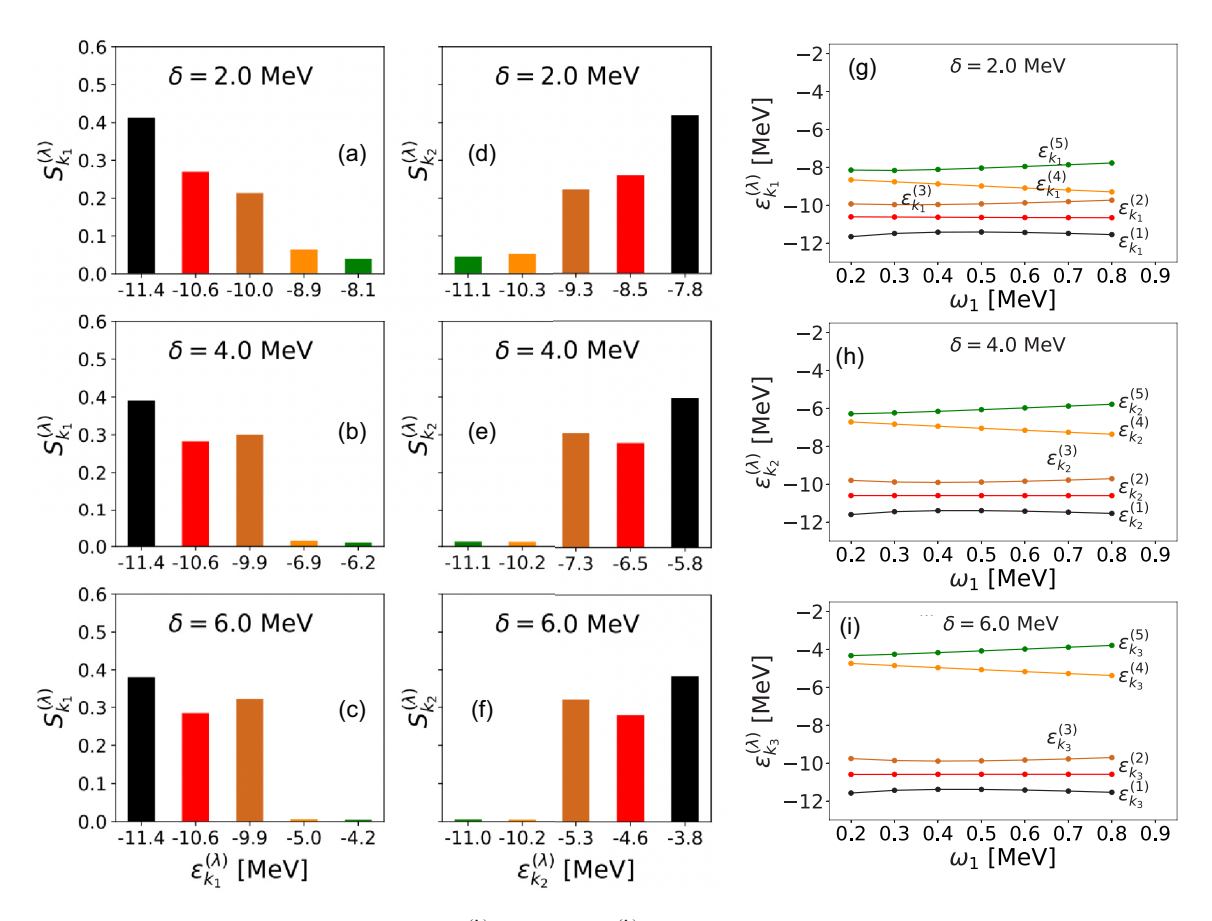


FIG. 12. The evolution of the spectroscopic factors $S_{k_1}^{(\lambda)}$ (a)–(c) and $S_{k_2}^{(\lambda)}$ (d)–(f) with the parameter δ at the fixed phonon frequency $\omega_1=0.4$ MeV, and of the fragment energies $\varepsilon_{k_1}^{(\lambda)}$ with the phonon frequency ω_1 for $\delta=2.0$ MeV (g), 4.0 MeV (h), and 6.0 MeV (i), at T=2 MeV.

where i = 1, 2. As before, we suppose the state k_1 to be the state $1f_{7/2}$ in the ⁷⁰Ni nucleus and set all the phonon vertices equal to 0.2 MeV. We first computed the spectroscopic factors $S_{k_1}^{(\lambda)}$ and $S_{k_2}^{(\lambda)}$ for the fixed temperature T=1 MeV, at which the chemical potential $\mu = -6.114$ MeV and the RMF energy $\varepsilon_{k_1} = -17.296$ MeV. The energy of the second state k_2 is also fixed as $\varepsilon_{k_2} = \varepsilon_{k_1} + \delta$, where $\delta = 2.0$ MeV. Thus, a smaller (larger) value of δ indicates a smaller (larger) energy distance between the states k_2 and k_1 . The left (middle) panels of Fig. 11 display the evolution of the spectroscopic factors $S_{k_1}^{(\lambda)}$ $(S_{k_0}^{(\lambda)})$ with the phonon frequency ω_1 at T=1 for the case of $\delta = 2.0$ MeV. From that, one obtains the critical phonon frequency ω_1^{crit} of 0.3 MeV. This is in accordance with the observation that the fragment energies $\varepsilon_{k_1}^{(1,2,3)}$ ($\varepsilon_{k_2}^{(3,4,5)}$) are closest to each other at $\omega_1=0.3$ MeV, as demonstrated in Fig. 11(g) [11(h)]. A comparison between the left and middle panels of Fig. 11 shows an apparent mirror symmetry between the two spectroscopic strength distributions. This symmetry occurs as a consequence of the single-valued phonon vertices, leading to the symmetry between the mass operators $\Sigma_{k_1}^e$ and $\Sigma_{k_2}^e$ with respect to the interchange $k_1 \leftrightarrow k_2$ [see Eqs. (A5) and (A6)].

Next, we increased the temperature T to 2 MeV and let the parameter δ take the values of 2.0, 4.0, and 6.0 MeV. Figures 12(a)–12(f) display the spectroscopic factors $S_{k_1}^{(\lambda)}$ and $S_{k_2}^{(\lambda)}$ at T=2 MeV for various values of δ and fixed phonon

frequency $\omega_1=0.4$ MeV. One can notice that the mirror symmetry between the two spectroscopic strength distributions persists for larger δ and higher temperature T. For several values of the parameter δ , the evolution of the fragment energies $\varepsilon_{k_1}^{(\lambda)}$ with the phonon frequency ω_1 at T=2 MeV is shown in Figs. 12(g)–12(i). Furthermore, one can see that the critical phonon frequency $\omega_1^{\rm crit}$ remains constant, i.e., 0.4 MeV, as one varies the parameter δ . Analogously to the first toy model, the critical phonon frequency $\omega_1^{\rm crit}$ increases roughly by 0.1 MeV per 1 MeV temperature increase, regardless the value of δ . From Fig. 12, one observes that the fragments with the energies $\varepsilon_{k_1}^{(1,2,3)}$ become more and more separated from those with $\varepsilon_{k_1}^{(4,5)}$ as the value of the parameter δ increases. Meanwhile, the sum of the spectroscopic factors $S_{k_1}^{(1,2,3)}$ exhausts the sum rule (21), as follows from Fig. 12.

3. Three-level model

In the third toy model, we consider a system which consists of three states k_1 , k_2 , and k_3 , as shown in Fig. 13, and one phonon mode with the frequency ω_1 . The energies of both states k_1 and k_3 are fixed, while the state k_2 is separated by the energy δ from the state k_1 . As before, we associate the states k_1 and k_3 with the states $1f_{7/2}$ and $2p_{1/2}$ in the nucleus 70 Ni. At T=1 MeV, the RMF energy of the state $2p_{1/2}$ is -8.717 MeV. We again set all the phonon vertices equal

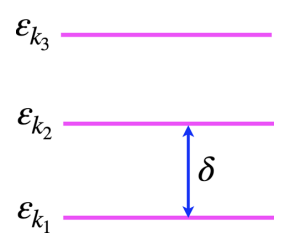


FIG. 13. The three states k_1 , k_2 , and k_3 in the third toy model. The parameter δ refers to the energy difference between the states k_1 and k_2 .

to 0.2 and keep the energy difference between the states k_1 and k_3 as ≈ 8.0 MeV. In this setting, it is instructive to vary the parameter δ and explore the sensitivity of the results to the relative position of the state k_2 . Thus, by varying δ , one can confront the cases of closed-shell and open-shell nuclear systems. In this toy model we consider the values of δ equal to 0.5, 4.0, and 8.0 MeV.

In the case of $\delta = 4.0$ MeV, when the state k_2 is located approximately in the middle between the states k_1 and k_3 , all of the mean-field states exhibit a similar fragmentation pattern in all temperature regimes and at various phonon frequencies. For example, all of the three mean-field states are weakly fragmented, as can be seen in Figs. 14(a)-14(c), and exhibit a manifestly dominant fragment with the spectroscopic factor around 0.6.

In contrast, for the case of $\delta = 0.5$ MeV, when the states k_1 and k_2 get close to each other, they are strongly fragmented, whereas the state k_3 is weakly fragmented, as displayed in Figs. 14(d)–14(f). This case illustrates the situation when the states k_1 and k_2 belong to the same major shell and become strongly mixed by the PVC. The third state k_3 belongs to the next major shell, thus becoming relatively isolated and, therefore, less affected by the PVC.

For $\delta=8.0$ MeV the states k_2 and k_3 are strongly fragmented, leaving the state k_1 weakly fragmented, as shown in Figs. 14(g) - 14(i). Here the states k_2 and k_3 would belong to the same major shell, while the state k_1 would be separated by an energy gap with the previous major shell. Thus, the situation mirrors the case of $\delta=0.5$ MeV.

From the second and third toy models, one thus obtains the most instructive information which helps us understand why the fragmentation patterns are different for different mean-field states and different PVC regimes. We conclude, in particular, that the degree of fragmentation of each state is sensitive to its relative distance from the neighboring mean-field states, if they are connected by the PVC mechanism. Overall, the neighboring states, which are closer to each other, are more strongly fragmented. The low-frequency phonons with larger coupling vertices contribute most significantly to the fragmentation, as in the case of zero temperature. However, the evolution of the phonon spectra with temperature affects indirectly the fragmentation of the single-particle states. For

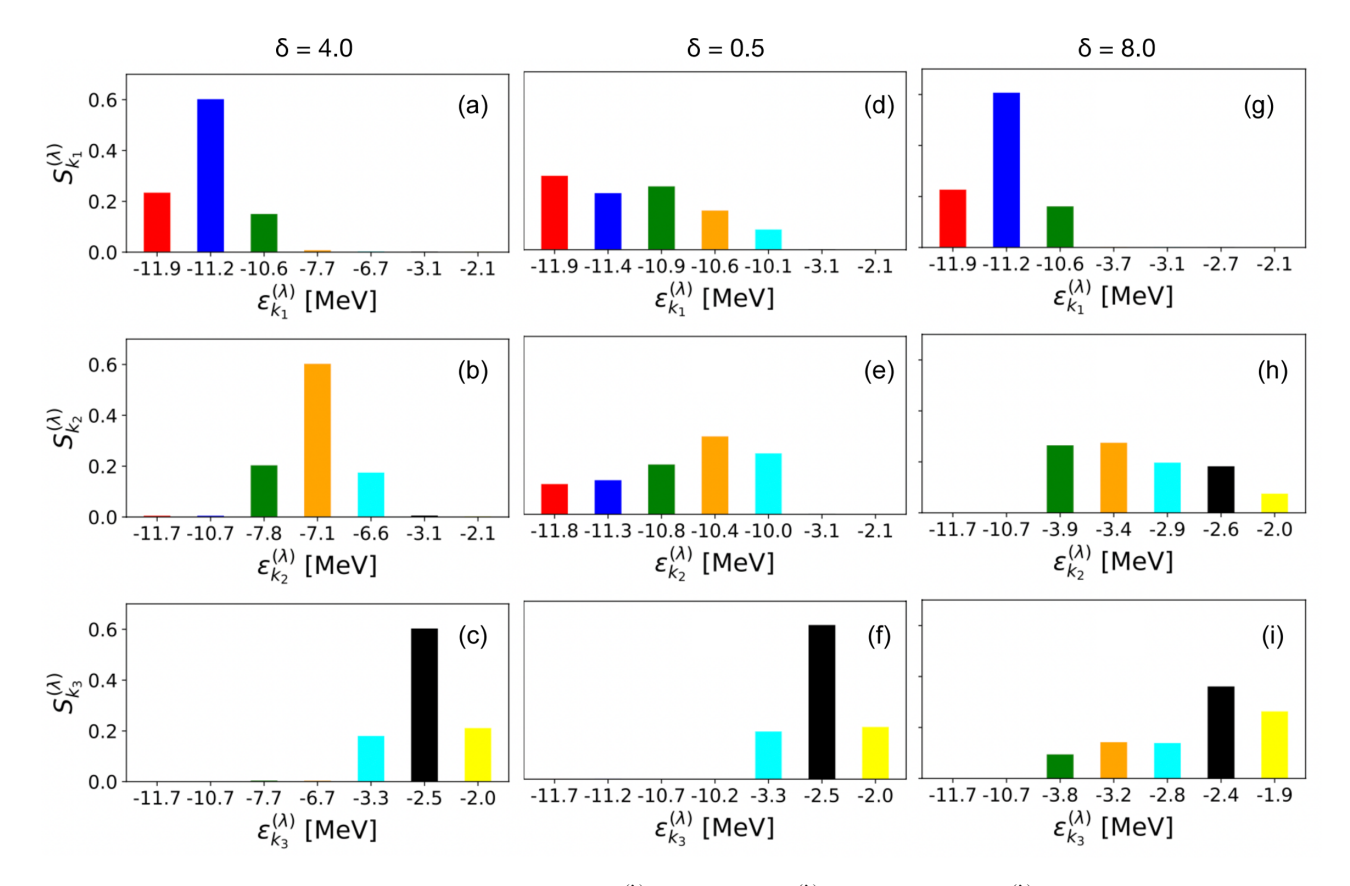


FIG. 14. The spectroscopic factors of the energy fragments $\varepsilon_{k_1}^{(\lambda)}$ [(a), (d), (g)], $\varepsilon_{k_2}^{(\lambda)}$ [(b), (e), (h)], and $\varepsilon_{k_3}^{(\lambda)}$ [(c), (f), (i)], where $\lambda=1,\ldots,7$, for the constant phonon frequency $\omega_1=0.5$ MeV and various values of the parameter δ . The temperature is equal to 1 MeV.

instance, more phonons with low frequencies appear at higher temperatures due to thermal unblocking, as shown in Ref. [5], and their coupling vertices, starting from small values, further grow with the temperature increase. Finite temperature thus introduces another dimension in the fragmentation pattern, that may have an impact on the important nuclear properties, such as symmetry energy, which is discussed in Sec. IV C.

- Y. Alhassid, B. Bush, and S. Levit, Thermal Shape Fluctuations, Landau Theory, and Giant Dipole Resonances in Hot Rotating Nuclei, Phys. Rev. Lett. 61, 1926 (1988).
- [2] Y. Alhassid and B. Bush, Orientation Fluctuations and the Angular Distribution of the Giant-Dipole-Resonance γ Rays in Hot Rotating Nuclei, Phys. Rev. Lett. **65**, 2527 (1990).
- [3] D. Kusnezov, Y. Alhassid, and K. A. Snover, Scaling Properties of the Giant Dipole Resonance Width in Hot Rotating Nuclei, Phys. Rev. Lett. 81, 542 (1998).
- [4] E. Litvinova and H. Wibowo, Finite-Temperature Relativistic Nuclear Field Theory: An Application to the Dipole Response, Phys. Rev. Lett. 121, 082501 (2018).
- [5] H. Wibowo and E. Litvinova, Nuclear dipole response in the finite-temperature relativistic time-blocking approximation, Phys. Rev. C 100, 024307 (2019).
- [6] E. Litvinova, C. Robin, and H. Wibowo, Temperature dependence of nuclear spin-isospin response and beta decay in hot astrophysical environments, Phys. Lett. B 800, 135134 (2020).
- [7] M. Mumpower, R. Surman, G. McLaughlin, and A. Aprahamian, The impact of individual nuclear properties on r-process nucleosynthesis, Prog. Part. Nucl. Phys. 86, 86 (2016).
- [8] J. M. Lattimer, Impact of GW170817 for the nuclear physics of the EOS and the r-process, Ann. Phys. 411, 167963 (2019).
- [9] A. R. Raduta, F. Gulminelli, and M. Oertel, Stellar electron capture rates on neutron-rich nuclei and their impact on stellar core collapse, Phys. Rev. C 95, 025805 (2017).
- [10] H. Nagakura, S. Furusawa, H. Togashi, S. Richers, K. Sumiyoshi, and S. Yamada, Comparing treatments of weak reactions with nuclei in simulations of core-collapse supernovae, Astrophys. J. Suppl. Series 240, 38 (2019).
- [11] A. Pascal, S. Giraud, A. F. Fantina, F. Gulminelli, J. Novak, M. Oertel, and A. R. Raduta, Impact of electron capture rates for nuclei far from stability on core-collapse supernovae, Phys. Rev. C 101, 015803 (2020).
- [12] K. Langanke, G. Martínez-Pinedo, and R. Zegers, Electron capture in stars, Rep. Prog. Phys. **84**, 066301 (2021).
- [13] E. Litvinova and C. Robin, Impact of complex many-body correlations on electron capture in thermally excited nuclei around ⁷⁸Ni, Phys. Rev. C **103**, 024326 (2021).
- [14] P. Donati, P. M. Pizzochero, P. F. Bortignon, and R. A. Broglia, Temperature Dependence of the Nucleon Effective Mass and the Physics of Stellar Collapse, Phys. Rev. Lett. 72, 2835 (1994).
- [15] A. F. Fantina, P. Donati, and P. M. Pizzochero, Systematic thermal reduction of neutronization in core-collapse supernovae, Phys. Lett. B **676**, 140 (2009).
- [16] A. F. Fantina, J. Margueron, P. Donati, and P. M. Pizzochero, Nuclear energy functional with a surface-peaked effective mass: Global properties, J. Phys. G: Nucl. Part. Phys. 38, 025101 (2011).
- [17] M. L. Tiago, P. Kent, R. Q. Hood, and F. A. Reboredo, Neutral and charged excitations in carbon fullerenes from

- first-principles many-body theories, J. Chem. Phys. **129**, 084311 (2008).
- [18] J. I. Martinez, J. García-Lastra, M. López, and J. Alonso, Optical to ultraviolet spectra of sandwiches of benzene and transition metal atoms: Time dependent density functional theory and many-body calculations, J. Chem. Phys. 132, 044314 (2010).
- [19] D. Sangalli, P. Romaniello, G. Onida, and A. Marini, Double excitations in correlated systems: A many-body approach, J. Chem. Phys. 134, 034115 (2011).
- [20] P. Schuck and M. Tohyama, Self-consistent RPA and the timedependent density matrix approach, Eur. Phys. J. A 52, 307 (2016).
- [21] V. Olevano, J. Toulouse, and P. Schuck, A formally exact one-frequency-only Bethe-Salpeter-like equation. Similarities and differences between GW+BSE and self-consistent RPA, J. Chem. Phys. 150, 084112 (2019).
- [22] P. Schuck, D. S. Delion, J. Dukelsky, M. Jemai, E. Litvinova, G. Roepke, and M. Tohyama, Equation of motion method for strongly correlated fermi systems and extended RPA approaches, Phys. Rep. 929, 1 (2021).
- [23] W. H. Dickhoff and D. V. Neck, Many-Body Theory Exposed! (World Scientific, Singapore, 2005)
- [24] W. H. Dickhoff and C. Barbieri, Self-consistent Green's function method for nuclei and nuclear matter, Prog. Part. Nucl. Phys. 52, 377 (2004).
- [25] V. M. Galitski and A. B. Migdal, Application of quantum field theory methods to the many body problem, Sov. Phys. JETP 7, 96 (1958).
- [26] D. S. Koltun, Theory of mean removal energies for single particles in nuclei, Phys. Rev. C 9, 484 (1974).
- [27] E. Litvinova and P. Schuck, Toward an accurate strongly-coupled many-body theory within the equation-of-motion framework, Phys. Rev. C 100, 064320 (2019).
- [28] E. Litvinova and Y. Zhang, Many-body theory for quasiparticle states in superfluid fermionic systems, Phys. Rev. C 104, 044303 (2021).
- [29] D. R. Hartree, The wave mechanics of an atom with a non-coulomb central field. Part II. some results and discussion, Math. Proc. Cambridge Philos. Soc. **24**, 111 (1928).
- [30] V. Fock, Näherungsmethode zur lösung des quantenmechanischen mehrkörperproblems, Z. Phys. **61**, 126 (1930).
- [31] D. R. Hartree and W. Hartree, Self-Consistent Field, with Exchange, for Beryllium, Proc. R. Soc. London, Ser. A 150, 9 (1935).
- [32] D. Bohm and D. Pines, A Collective Description of Electron Interactions. 1. Magnetic Interactions, Phys. Rev. 82, 625 (1951).
- [33] L. P. Gor'kov, On the energy spectrum of superconductors, Sov. Phys. JETP 7, 505 (1958).
- [34] J. Bardeen, L. N. Cooper, and J. R. Schrieffer, Microscopic theory of superconductivity, Phys. Rev. 106, 162 (1957).
- [35] A. Bohr and B. R. Mottelson, *Nuclear Structure* (World Scientific, Singapore, 1969), Vol. 1.

- [36] A. Bohr and B. R. Mottelson, *Nuclear Structure* (Benjamin, New York, 1975), Vol. 2.
- [37] P. F. Bortignon, R. Broglia, D. Bes, and R. Liotta, Nuclear field theory, Phys. Rep. **30**, 305 (1977).
- [38] R. A. Broglia and P. F. Bortignon, Collective effects in the damping width of giant resonances, Phys. Lett. B 101, 135 (1981).
- [39] G. Bertsch, P. Bortignon, and R. Broglia, Damping of nuclear excitations, Rev. Mod. Phys. 55, 287 (1983).
- [40] V. Soloviev, *Theory of Atomic Nuclei: Quasiparticles and Phonons* (Institute of Physics, Bristol, 1992).
- [41] V. Yu. Ponomarev, P. F. Bortignon, R. A. Broglia, and V. V. Voronov, Microscopic studies of multi-phonon resonances, Nucl. Phys. A 687, 170 (2001).
- [42] D. Savran, M. Babilon, A. M. van den Berg, M. N. Harakeh, J. Hasper, A. Matic, H. J. Wörtche, and A. Zilges, Nature of the Pygmy Dipole Resonance in 140 Ce Studied in $(\alpha, \alpha' \gamma)$ Experiments, Phys. Rev. Lett. **97**, 172502 (2006).
- [43] F. Andreozzi, F. Knapp, N. Lo Iudice, A. Porrino, and J. Kvasil, Multiphonon nuclear response in ¹⁶O: A microscopic treatment equivalent to the shell model, Phys. Rev. C 78, 054308 (2008).
- [44] A. Idini, F. Barranco, and E. Vigezzi, Quasiparticle renormalization and pairing correlations in spherical superfluid nuclei, Phys. Rev. C **85**, 014331 (2012).
- [45] E. Litvinova, Pion-nucleon correlations in finite nuclei in a relativistic framework: Effects on the shell structure, Phys. Lett. B 755, 138 (2016).
- [46] C. Robin and E. Litvinova, Nuclear response theory for spin-isospin excitations in a relativistic quasiparticle-phonon coupling framework, Eur. Phys. J. A 52, 205 (2016).
- [47] C. Robin and E. Litvinova, Coupling charge-exchange vibrations to nucleons in a relativistic framework: Effect on Gamow-Teller transitions and β -decay half-lives, Phys. Rev. C **98**, 051301(R) (2018).
- [48] Y. Niu, Z. Niu, G. Colò, and E. Vigezzi, Interplay of quasiparticle-vibration coupling and pairing correlations on β -decay half-lives, Phys. Lett. B **780**, 325 (2018).
- [49] C. Robin and E. Litvinova, Time-Reversed Particle-Vibration Loops and Nuclear Gamow-Teller Response, Phys. Rev. Lett. 123, 202501 (2019).
- [50] V. Tselyaev, N. Lyutorovich, J. Speth, and P. G. Reinhard, Self-consistency in the phonon space of the particle-phonon coupling model, Phys. Rev. C 97, 044308 (2018).
- [51] N. Lyutorovich, V. Tselyaev, J. Speth, and P. G. Reinhard, Excitation spectra of exotic nuclei in a self-consistent phononcoupling model, Phys. Rev. C 98, 054304 (2018).
- [52] S. Shen, G. Colò, X. Roca-Maza *et al.*, Particle-vibration coupling for giant resonances beyond the diagonal approximation, Phys. Rev. C 101, 044316 (2020).
- [53] G. De Gregorio, J. Herko, F. Knapp, N. Lo Iudice, and P. Veselý, Ground-state correlations within a nonperturbative approach, Phys. Rev. C 95, 024306 (2017).
- [54] G. De Gregorio, F. Knapp, N. Lo Iudice, and P. Veselý, Lowand high-energy spectroscopy of ¹⁷O and ¹⁷F within a microscopic multiphonon approach, Phys. Rev. C 95, 034327 (2017).
- [55] F. Knapp, N. Lo Iudice, P. Veselý, F. Andreozzi, G. De Gregorio, and A. Porrino, Dipole response in ¹³²Sn within a self-consistent multiphonon approach, Phys. Rev. C **90**, 014310 (2014).
- [56] F. Knapp, N. Lo Iudice, P. Veselý, F. Andreozzi, G. De Gregorio, and A. Porrino, Dipole response in ²⁰⁸Pb within a

- self-consistent multiphonon approach, Phys. Rev. C **92**, 054315 (2015)
- [57] H. Wibowo, E. Litvinova, Y. Zhang, and P. Finelli, Temperature evolution of the nuclear shell structure and the dynamical nucleon effective mass, Phys. Rev. C 102, 054321 (2020).
- [58] E. Litvinova and P. Ring, Covariant theory of particlevibrational coupling and its effect on the single-particle spectrum, Phys. Rev. C 73, 044328 (2006).
- [59] E. Litvinova, Quasiparticle-vibration coupling in a relativistic framework: Shell structure of Z = 120 isotopes, Phys. Rev. C **85**, 021303(R) (2012).
- [60] B. D. Serot and J. D. Walecka, Advances in Nuclear Physics, edited by J. W. Negele and E. Vogt (Plenum Press, New York, 1986), Vol. 16.
- [61] B. D. Serot and J. Walecka, Properties of finite nuclei in a relativistic quantum field theory, Phys. Lett. B 87, 172 (1979).
- [62] P. Ring, Relativistic mean field theory in finite nuclei, Prog. Part. Nucl. Phys. 37, 193 (1996).
- [63] D. Vretenar, A. V. Afanasjev, G. A. Lalazissis, and P. Ring, Relativistic Hartree-Bogoliubov theory: static and dynamic aspects of exotic nuclear structure, Phys. Rep. 409, 101 (2005).
- [64] P. Ring and P. Schuck, The Nuclear Many-Body Problem (Springer-Verlag, Berlin, 1980).
- [65] J. Dukelsky, G. Röpke, and P. Schuck, Generalized Brückner-Hartree-Fock theory and self-consistent RPA, Nucl. Phys. A 628, 17 (1998).
- [66] P. Schuck, Mean-field theory for fermion pairs and the ab initio particle-vibration coupling approach, Eur. Phys. J. A 55, 250 (2019).
- [67] P. Ring and E. Werner, Distribution of single-particle strengths in the nuclei ²⁰⁷Tl, ²⁰⁷Pb, ²⁰⁹Bi and ²⁰⁹Pb, Nucl. Phys. A 211, 198 (1973).
- [68] I. Hamamoto and P. Siemens, Large effect of core polarization on the single-particle spectra around ²⁰⁸Pb, Nucl. Phys. A 269, 199 (1976).
- [69] R. P. J. Perazzo, S. L. Reich, and H. M. Sofía, Renormalization of particle and hole states in ²⁰⁸Pb, Nucl. Phys. A 339, 23 (1980).
- [70] V. Bernard and N. Van Giai, Effects of collective modes on the single-particle states and the effective mass in ²⁰⁸Pb, Nucl. Phys. A 348, 75 (1980).
- [71] C. Mahaux, P. Bortignon, R. Broglia, and C. Dasso, Dynamics of the shell model, Phys. Rep. 120, 1 (1985).
- [72] M. Jaminon and C. Mahaux, Effective masses in relativistic approaches to the nucleon-nucleus mean field, Phys. Rev. C 40, 354 (1989).
- [73] G. Colò, H. Sagawa, and P. F. Bortignon, Effect of particlevibration coupling on single-particle states: A consistent study within the Skyrme framework, Phys. Rev. C 82, 064307 (2010).
- [74] L.-G. Cao, G. Colò, H. Sagawa, and P. F. Bortignon, Properties of single-particle states in a fully self-consistent particlevibration coupling approach, Phys. Rev. C 89, 044314 (2014).
- [75] D. J. Dean, S. E. Koonin, K. Langanke, and P. B. Radha, Temperature dependence of the nuclear symmetry energy, Phys. Lett. B **356**, 429 (1995).
- [76] A. F. Fantina, P. Blottiau, J. Margueron, P. Mellor, and P. M. Pizzochero, Effects of the temperature dependence of the inmedium nucleon mass on core-collapse supernovae, Astron. Astrophys. 541, A30 (2012).
- [77] D. J. Dean, K. Langanke, and J. M. Sampaio, Temperature dependence of the symmetry energy, Phys. Rev. C 66, 045802 (2002).

- [78] T. Matsubara, A new approach to quantum-statistical mechanics, Prog. Theor. Phys. 14, 351 (1955).
- [79] A. A. Abrikosov, L. P. Gorkov, and I. E. Dzyaloshinski, *Methods of Quantum Field Theory in Statistical Physics* (Dover, New York, 1975).
- [80] A. Zagoskin, *Quantum Theory of Many-Body Systems*, Graduate Texts in Physics (Springer International, Cham, 2014).
- [81] E. Litvinova and H. Wibowo, Nuclear response in a finitetemperature relativistic framework, Eur. Phys. J. A 55, 223 (2019).
- [82] G. A. Lalazissis, J. König, and P. Ring, New parametrization for the Lagrangian density of relativistic mean field theory, Phys. Rev. C 55, 540 (1997).
- [83] P. Ring, Z.-Y. Ma, N. Van Giai, D. Vretenar, A. Wandelt, and L.-G. Cao, The time-dependent relativistic mean-field theory and the random phase approximation, Nucl. Phys. A 694, 249 (2001).
- [84] B. L. Birbrair and V. I. Ryazanov, Theory of doorway states for one-nucleon-transfer reactions, Phys. At. Nucl. 63, 1753 (2000).
- [85] N. Paar, P. Ring, T. Nikšić, and D. Vretenar, Quasiparticle random phase approximation based on the relativis-

- tic Hartree-Bogoliubov model, Phys. Rev. C **67**, 034312 (2003)
- [86] E. Litvinova and P. Schuck, Nuclear superfluidity at finite temperature, Phys. Rev. C 104, 044330 (2021).
- [87] R. A. Broglia and V. Zelevinsky, *Fifty Years of Nuclear BCS* (WORLD SCIENTIFIC, Singapore, 2013).
- [88] G. Audi, A. H. Wapstra, and C. Thibault, The AME2003 atomic mass evaluation: (II) Tables, graphs, and references, Nucl. Phys. A 729, 337 (2003).
- [89] V. Vaquero *et al.*, Fragmentation of Single-Particle Strength Around the Doubly Magic Nucleus ¹³²Sn and the Position of the $0f_{5/2}$ Proton-Hole State in ¹³¹In, Phys. Rev. Lett. **124**, 022501 (2020).
- [90] E. Litvinova, P. Ring, and V. Tselyaev, Particle-vibration coupling within covariant density functional theory, Phys. Rev. C 75, 064308 (2007).
- [91] N. Van Giai and P. V. Thieu, Radial and energy dependences of the nucleon effective mass in ²⁰⁸Pb, Phys. Lett. B 126, 421 (1983).
- [92] Z. Ma and J. Wambach, Implications of a dynamical effective mass on the nuclear shell model, Nucl. Phys. A 402, 275 (1983).